

Mass-stream trajectories with non-synchronously rotating donors

D. D. Hendriks¹  , R. G. Izzard¹ 

¹*Department of Physics, University of Surrey, Guildford, GU2 7XH, Surrey, UK*

Accepted 2023 July 6. Received 2023 July 5; in original form 2023 June 5

ABSTRACT

Mass-transfer interactions in binary stars can lead to accretion disk formation, mass loss from the system and spin-up of the accretor. To determine the trajectory of the mass-transfer stream, and whether it directly impacts the accretor, or forms an accretion disk, requires numerical simulations. The mass-transfer stream is approximately ballistic, and analytic approximations based on such trajectories are used in many binary population synthesis codes as well as in detailed stellar evolution codes. We use binary population synthesis to explore the conditions under which mass transfer takes place. We then solve the reduced three-body equations to compute the trajectory of a particle in the stream for systems with varying system mass ratio, donor synchronicity and initial stream velocity. Our results show that on average both more mass and more time is spent during mass transfer from a sub-synchronous donor than from a synchronous donor. Moreover, we find that at low initial stream velocity the asynchronous rotation of the donor leads to self-accretion over a large range of mass ratios, especially for super-synchronous donors. The stream (self-)intersects in a narrow region of parameter space where it transitions between accreting onto the donor or the accretor. Increasing the initial stream velocity leads to larger areas of the parameter space where the stream accretes onto the accretor, but also more (self-)intersection. The radii of closest approach generally increase, but the range of specific angular momenta that these trajectories carry at the radius of closest approach gets broader. Our results are made publicly available.

Key words: binaries: close – stars: mass-loss – accretion

1 INTRODUCTION

Binary stellar systems are ubiquitous and the proximity of a star to a companion introduces a variety of interactions. These interactions lead to a range of phenomena like the stripping of the outer envelope of a star and the transfer of mass and angular momentum (Lubow & Shu 1975; Ulrich & Burger 1976), tidal interactions (Zahn 1977b, 2008; Ogilvie 2014; Mirouh et al. 2023), the formation and evolution of accretion disks (Pringle & Rees 1972; Shakura & Sunyaev 1973; Papaloizou & Pringle 1977; Osaki et al. 1993; Hameury 2020), accretion induced supernovae (Nomoto 1986; Ruiter et al. 2010; Claeys et al. 2014), the (high velocity) ejection of companions (Blaauw 1961; Tauris & Takens 1998; Renzo et al. 2019), quasi chemically-homogeneous evolution (Ghodla et al. 2023), Be stars (Shao & Li 2014; Postnov et al. 2015), and circumbinary disk formation (Kashi & Soker 2011; Pejcha et al. 2016; Izzard & Jermyn 2022).

A comprehensive review of these binary interactions is given in De Marco & Izzard (2017), but the most relevant interactions to the current study are the transfer of mass and tidal interactions between the stars. Both these interchange orbital and rotational angular momentum of the system and the stars. Tidal interactions circularise the orbit, i.e. reduce the eccentricity, and synchronise the stars, i.e. force the stellar rotation rate to equal the orbital rotation rate. Mass transfer, among other effects, de-synchronises the stars by angular momentum transfer from the donor to the accretor.

In a semi-detached system, where the accretor significantly underfills its Roche-Lobe, the mass transfer process can be split into three

main parts: The ejection from the donor, the flight of the particles in the potential between the stars, and the accretion onto the accretor Kruszewski (1964b). During the flight stage, the gravitational interaction between the binary system and the particle leads to a torque and subsequent exchange of angular momentum between the binary system and the particle. It is during this stage that the final outcome of the trajectory is determined, i.e. accretion onto the companion star, accretion back onto the donor star or loss from the system entirely. The flight stage is approximately ballistic, and it is the stage that we focus on in this study.

The potential that is used to calculate when and how mass is transferred from one star to the other is often calculated under the assumption that the orbit of the binary system is circular and that the donor rotates synchronously with the orbit (Lubow & Shu 1975). Together with the approximation that the stars are point particles this setup is often called the Roche potential (Fig. 1).

The points in this potential where accelerations vanish are called Lagrange points. The first Lagrange point lies on the critical equipotential surface and is located between the two stars. While generalisations of the equipotential surface and the inclusion of additional physical effects have been studied, binary stellar-evolution codes often still use simplified analytical formulae for the mass stream properties based on circular and synchronous systems. Some examples of extensions to this simple Roche model that relax some assumptions, or add additional physics, are those that allow the asynchronous rotation of the donor with respect to the orbital rotation (Plavec 1958; Limber 1963; Kruszewski 1963), eccentric orbits (Avni 1976; Sepinsky et al. 2007), spin-orbit misalignment (Limber 1963; Avni & Schiller 1982), effects of external radiation (Podsiadlowski & Rees

* E-mail: dh00601@surrey.ac.uk (DDH)

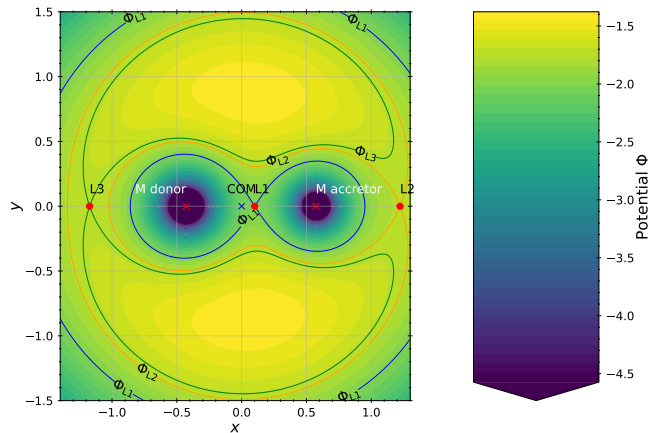


Figure 1. The Roche potential, Φ , in the co-rotating frame of reference, with the positions of the two stars and the centre of mass denoted with red and blue crosses respectively. We indicate several equilibrium points within the co-rotating frame of reference, the L1, L2 and L3 Lagrange points, by red dots. The lines of constant potential energy that belong to each of these points are indicated with the solid blue, orange and green lines and labelled Φ_{L1} , Φ_{L2} , and Φ_{L3} respectively. The colour-scale indicates the potential. The system is characterised by two masses of which the ratio of the accretor to the donor mass is $q_{\text{acc}} = 0.75$. Moreover, the ratio of the rotation rate of the donor to the orbital rotation rate is $f_{\text{sync}} = 1$

1994; Drechsel et al. 1995; Phillips & Podsiadlowski 2002; Tsantilas & Rovithis-Livaniou 2006; Dermine et al. 2009) or combinations of these (Vanbeveren 1977). These extensions change the shape of the critical surface and the location of the Lagrange points, most notably the first.

Asynchronous rotation of the donor induces time-dependent tides, exerted by the companion, which then affect the potential. The above-mentioned extensions that take the asynchronous rotation of the donor into account (e.g. Plavec 1958; Limber 1963; Kruszewski 1963) rest on several assumptions. First, the shape of the donor is assumed to conform instantaneously to the shape dictated by the potential. Secondly, the motion of mass in the donor is assumed to move primarily along the axis of rotation (i.e. primarily zonal, instead of meridional). These two assumptions are called the first approximation (Limber 1963; Savonije 1978; Sepinsky et al. 2007). Asynchronous rotation of the donor can occur due to, e.g., rapid expansion of the donor star leading to sub-synchronous rotation when it fills its Roche Lobe.

Given L1 it is possible to calculate the initial conditions and subsequent trajectory of the mass flow away from the donor star. Lubow & Shu (1975) analyse the behaviour of donor material at L1 and the trajectory of the stream of matter flowing from L1 to the accretor. Their perturbative analysis provides mass-transfer stream properties over a range of orbital configurations of the binary based on ballistic trajectories of particles in the Roche potential. Critical to the study of Lubow & Shu (1975) are the assumptions that the donor rotates synchronously with the orbit, that the stream at L1 has a low thermal-velocity (cold) of compared to the orbital velocity, that the gas remains isothermal throughout the flow, and that the mass contained in the stream is negligible compared to the total mass of the system. Ulrich & Burger (1976) provide analytical fits to this data and study the response of the accretor when the mass-transfer stream either directly impacts the accretor or misses the accretor and forms an accretion disk. Kruszewski (1963, 1964a,b, 1967) calculates properties of the mass transfer in non-synchronous rotating donors,

including the effects of kinematic acceleration due to the bulging motion of the donor star as a result of its non-synchronicity. Warner & Peters (1972) and Flannery & Faulkner (1975) study the effect of initial thermal-velocity of the stream particles on the location of hotspots in cataclysmic variable systems. Sepinsky et al. (2010) and Davis et al. (2013, 2014) calculate the ballistic trajectories to include in their osculating orbit calculations and consider asynchronous rotating donors. They do not make the results of these calculations public, however.

The aim of our paper is to publicly release interpolation tables that contain the results of our ballistic-stream trajectories calculations over a wide range of mass ratios and degrees of asynchronicity of the donor, as well as mass-stream surface areas and initial thermal velocities at L1. These can be used in combination with osculating orbit calculations (Davis et al. 2013, 2014; Dosopoulou & Kalogera 2016; Dosopoulou et al. 2017), and as tables in stellar evolution codes like MESA (Jermyn et al. 2023) and population synthesis codes like BINARY_C (Izzard & Jermyn 2022) or COMPAS (Riley et al. 2022).

Our paper is structured as follows. In Section 2 we explain the theoretical basis of our project, and in Section 3 we lay out the methods used to calculate our ballistic trajectories and our approach to dataset interpolation. In Section 4 we show the results of our ballistic trajectory calculations for several initial properties of the mass transfer stream. We discuss and conclude in Sections 5 and 6. Appendix A provides a description of our interpolation datasets, and Appendix B contains a visual overview of the first three Lagrange point locations in two different frames of reference.

2 THEORY

In this section we lay out the theoretical basis of the calculations of the trajectory of a particle flowing through L1. We first determine the potential that the particle experiences when attached to the donor star and when moving freely through the system, and we then determine the cross-sectional surface area of the stream and the initial velocity of the particles L1.

2.1 Generalised Roche potential and Lagrange points

To calculate the particle trajectory through the potential of the binary system, we consider the reduced three-body problem in a Cartesian coordinate system $Oxyz$ in the co-rotating frame of the binary, which rotates with angular frequency ω , with the origin O of the frame of reference located on the centre of mass of the system (Hubová & Pejcha 2019). The x -coordinate is defined parallel to the line connecting the centres of the stars, the y -coordinate defined perpendicular to the x -coordinate and in the plane of the orbit and the z -coordinate perpendicular to the orbital plane. Throughout our calculations we consider particle motion only in the plane of the orbit, i.e. $z = 0$.

The donor and accretor are regarded as point masses, M_{don} and M_{acc} , with their positions fixed at $\mathbf{x}_{\text{don}} = [-\mu_{\text{acc}}, 0]$ and $\mathbf{x}_{\text{acc}} = [1 - \mu_{\text{acc}}, 0]$ respectively, where $\mu_{\text{acc}} = M_{\text{acc}} / (M_{\text{don}} + M_{\text{acc}})$, and $q_{\text{acc}} = M_{\text{acc}} / M_{\text{don}}$. Our units of length, time, velocity, and potential are the semi-major axis a , the inverse orbital frequency ω^{-1} , the orbital velocity $a\omega$, and $a^2\omega^2$ respectively, unless otherwise indicated.

A particle freely moving in a binary star system in a co-rotating frame experiences the gravitational potential of both stars, and a centrifugal potential due to the co-rotation, and a Coriolis force due to movement relative to the co-rotating frame. When we assume that both stars are centrally condensed, i.e. the Roche model, the potential

is,

$$\Phi(x, y) = -\frac{\mu_{\text{acc}}}{[(x-1+\mu_{\text{acc}})^2+y^2]^{1/2}} - \frac{1-\mu_{\text{acc}}}{[(x+\mu_{\text{acc}})^2+y^2]^{1/2}} - \frac{1}{2}(x^2+y^2). \quad (1)$$

This is valid for a freely moving particle, i.e. not inside either star, because there is no other force acting on the particle. This potential is also valid to calculate the critical surface beyond which mass starts flowing away from the donor, in the case the donor rotates synchronously with the orbit and its rotation is along an axis parallel to the orbital rotation. We show an example of the Roche potential in Fig. 1.

To calculate the location at which mass starts flowing from the donor we need to find the critical surface of the donor, i.e. the last surface at which the net inward force of the potential is balanced by the pressure of the star. We assume the rotation of the donor is in the same direction as the orbit of the binary system, the dynamic timescale is shorter than the tidal timescale, and that the orbit is circular, in the rest of our study. The potential felt by a non-synchronously rotating donor is

$$\Phi_{\text{don}}(x, y, f_{\text{sync}}) = -\frac{\mu_{\text{acc}}}{[(x-1+\mu_{\text{acc}})^2+y^2]^{1/2}} - \frac{1-\mu_{\text{acc}}}{[(x+\mu_{\text{acc}})^2+y^2]^{1/2}} - \frac{1}{2}f_{\text{sync}}^2(x^2+y^2) - (f_{\text{sync}}^2-1)\mu x. \quad (2)$$

Here the potential acting on the donor depends on the synchronicity factor,

$$f_{\text{sync}} = \Omega_{\text{don}}/\omega, \quad (3)$$

where Ω_{don} is the rotation rate of the donor.

We calculate the location of the first three Lagrange points of the donor, determining the critical equipotential surface, by taking the derivative of the potential in equation 2 with respect to x and setting $y = 0$,

$$\frac{d\Phi_{\text{don}}(y=0)}{dx} = \frac{(1-\mu_{\text{acc}})}{(\mu_{\text{acc}}+x)^2} + \frac{\mu_{\text{acc}}}{(\mu_{\text{acc}}+x-1)^2} - f_{\text{sync}}^2x - \mu_{\text{acc}}(f_{\text{sync}}^2-1) = 0. \quad (4)$$

We solve this equation for x which gives the first three Lagrange points. In Section B we show these points for a selection of f_{sync} .

In the potential acting on particles in the donor (equation 2) we assume that the dynamical timescale of the donor is much shorter than the timescale of the tides induced by the secondary star and the non-synchronous rotation of the donor (Limber 1963; Sepinsky et al. 2007), and thus the potential is approximately static. We express the validity of this approximation as

$$\eta_{\text{static}} = \frac{P_{\text{orb}}}{\tau_{\text{dyn, don}}\alpha(e, f, \nu)} \gg 1, \quad (5)$$

where P_{orb} is the orbital period of the system, $\tau_{\text{dyn, don}} = \sqrt{R^3/2GM_{\text{don}}}$ is the dynamical timescale of the donor where R is its radius and M_{don} is its mass, G is the gravitational constant, and

$$\alpha(f, e=0, \nu=0) = |1-f_{\text{sync}}| \quad (6)$$

is generally a function of synchronicity f_{sync} , eccentricity e and mean anomaly ν , but here we focus on circular systems (i.e. $e=0$, ν is irrelevant) (Sepinsky et al. 2007). $\alpha = \tau_{\text{tide}}\omega/2\pi$ captures the

timescale, τ_{tide} , on which tides induced by asynchronous rotation operate. If $\eta_{\text{static}} \gg 1$, the response of the donor to a change in the potential is much faster than the timescale of the tides induced by the asynchronous rotation of the donor. The potential can then be regarded as static.

2.2 Mass-stream particle properties

In this section we describe the relevant properties of the particles in the mass stream at and around the first Lagrange point, L1.

2.2.1 Thermal velocity of stream particles at L1

The initial velocity with which material flows through L1 is set by the thermal velocity of the material at L1 (Warner & Peters 1972; Lubow & Shu 1975; Flannery & Faulkner 1975). The thermal velocity, v_{thermal} , depends on the properties of the photosphere of the donor,

$$v_{\text{thermal}} = \tilde{v}_{\text{thermal}}/a\omega = \sqrt{\frac{3kT_{\text{eff, don}}}{m}} \frac{1}{a\omega} = \sqrt{\frac{3kT_{\text{eff, don}}}{\mu_{\text{phot, don}}m_a}} \frac{1}{a\omega}, \quad (7)$$

where $\tilde{v}_{\text{thermal}}$ is the dimensionful thermal velocity, k is the Boltzmann constant, $T_{\text{eff, don}}$ is the effective temperature of the donor, m and $\mu_{\text{phot, don}}$ are the average mass and the mean molecular weight of the particles in the photosphere respectively, m_a is the atomic mass unit, a is the semi-major axis of the system and ω is the orbital frequency of the system. Here we have assumed the equation of state behaves like an ideal gas.

2.2.2 Stream surface area at L1

The mass-transfer stream at L1 has a non-zero surface area such that particles are distributed around L1. We calculate the surface area of the stream, A_{stream} (Meyer & Meyer-Hofmeister 1983; Ritter 1988; Davis et al. 2013, 2014), assuming a circular cross-section, as,

$$A_{\text{stream}} = \tilde{A}_{\text{stream}}/a^2 = \frac{2\pi k T_{\text{eff, don}}}{\mu_{\text{phot, don}}m_a} \frac{q_{\text{acc}}}{\mu_{\text{acc}}\omega^2} \times \left\{ g(q_{\text{acc}}) \left[g(q_{\text{acc}}) - (1+q_{\text{acc}})f_{\text{sync}}^2 \right] \right\}^{-1/2} \frac{1}{a^2}, \quad (8)$$

where $\tilde{A}_{\text{stream}}$ is the dimensionful stream area, f_{sync} is the synchronicity factor (equation 3). The geometric factor, $g(q_{\text{acc}})$, is,

$$g(q_{\text{acc}}) = \frac{1}{d_{\text{L1, don}}^3} + \frac{q_{\text{acc}}}{(1-d_{\text{L1, don}})^3}, \quad (9)$$

where $d_{\text{L1, don}}$ is the distance from the centre of the donor to L1 in terms of the separation of the binary system. We reformulate the mass stream area in terms of the thermal-velocity of the particle v_{thermal} at L1, as,

$$A_{\text{stream}} = \frac{2\pi}{3} v_{\text{thermal}}^2 (1+q_{\text{acc}}) \times \left\{ g(q_{\text{acc}}) \left[g(q_{\text{acc}}) - (1+q_{\text{acc}})f_{\text{sync}}^2 \right] \right\}^{-1/2}. \quad (10)$$

Fig. 2 (a) shows the stream diameter, D_{stream} , as a function of the thermal-velocity, v_{thermal} , mass ratio and synchronicity factor. The solid line indicates $q_{\text{acc}} = 1$ and $f_{\text{sync}} = 1$, and the grey transparent

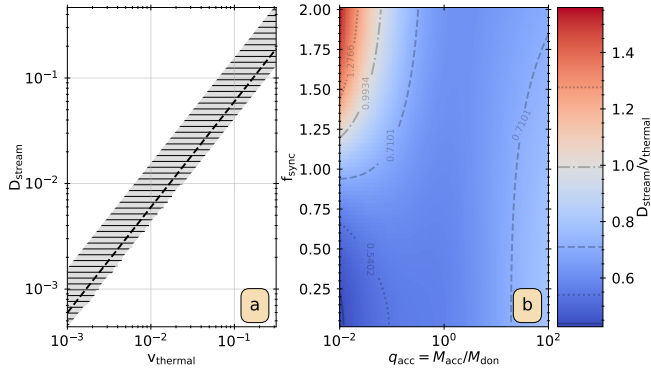


Figure 2. (a): The diameter of the mass-stream, D_{stream} (ordinate), as a function of the thermal-velocity, v_{thermal} (abscissa). The black dashed line indicates the mass-stream diameter for $q_{\text{acc}} = 1$ and $f_{\text{sync}} = 1$, and the grey horizontal-dashed region indicates the range of D_{stream} spanned by the ranges of q_{acc} and f_{sync} adopted in our study. (b): Ratio of D_{stream} to v_{thermal} as a function of mass ratio q_{acc} (abscissa) and synchronicity factor f_{sync} (ordinate).

area indicates the extent of diameters spanned by the ranges of q_{acc} and f_{sync} . At fixed thermal-velocity, the extent of stream diameters spans about a factor of 3 – 4, and from $v_{\text{thermal}} \gtrsim 0.06$ the diameter of the stream reaches a significant fraction ($D_{\text{stream}} \gtrsim 0.1$) of the separation of the system. Fig. 2 (b) shows the ratio of the stream diameter and the thermal-velocity as a function of mass ratio q_{acc} and f_{sync} . Overall, in most of the parameter space this ratio does not exceed ≈ 0.7 , except for $f_{\text{sync}} > 1.1$ and $q_{\text{acc}} < 10^{-1}$. Only in the extreme case of $f_{\text{sync}} \gtrsim 1.5$ and $q_{\text{acc}} \approx 10^{-2}$ does the ratio exceed unity, indicating that for most of the parameter space, the stream diameter is close to that of the case of a synchronous and equal mass-ratio system.

The density distribution in the stream at L1 is approximately Gaussian (Lubow & Shu 1975; Raymer 2012),

$$\xi(\tilde{l}) = \eta e^{-\tilde{l}^2/2\sigma^2}, \quad (11)$$

where reduced position offset $|\tilde{l}| < 1$ and position offset $l = \tilde{l}\sqrt{A/\pi}$ $\sigma = 0.4$ such that at $l = \pm 1$ the density equals that of the photosphere of the donor (Davis et al. 2014), and,

$$\eta = \frac{1}{\int_{-1}^1 \xi(\tilde{l}) d\tilde{l}}. \quad (12)$$

In a given system with q_{acc} , f_{sync} and v_{thermal} , we calculate trajectories with $N_{A\text{stream}}$ equally-spaced initial positions relative to L1, sampled in the range $[-D_{\text{stream}}/2, D_{\text{stream}}/2]$, and weigh each according to equation 11. We use these trajectories to calculate averaged quantities.

3 METHOD

In this section we explain how we calculate the trajectory of a particle and how we classify its trajectory in the potential of Section 2.1, as well how we calculate the relevant properties of mass transfer in a binary population.

3.1 Particle trajectories in the Roche potential

In the following sections we explain our method of calculating the trajectory of particles in the Roche potential.

3.1.1 Reduced three-body equations and ballistic integration

The trajectory of a particle is found by integrating the equations of motion of the particle in the rotating frame,

$$\ddot{x} = -\frac{\partial\Phi}{\partial x} + 2\dot{y} \quad (13)$$

and

$$\ddot{y} = -\frac{\partial\Phi}{\partial y} - 2\dot{x}, \quad (14)$$

where x and y are the position components of the particle with respect to the centre of mass of the binary system, \dot{x} and \dot{y} the velocity components of the particle, and \ddot{x} and \ddot{y} the acceleration components of the particle, and Φ is the potential experienced by the particle (equation 1). The first terms in equations 13 and 14 are the gradient of the potential and the second terms are the Coriolis force in each direction.

We calculate the specific energy and angular momentum of the particle in the inertial frame, with respect to the centre of mass, using quantities defined in the co-rotating frame,

$$\varepsilon = \Phi + \frac{1}{2}(\dot{x}^2 + \dot{y}^2) + x^2 + y^2 + x\dot{y} - \dot{x}y \quad (15)$$

and

$$h = x^2 + y^2 + x\dot{y} - \dot{x}y, \quad (16)$$

respectively, in units $a^2\omega^2$ and $a^2\omega$.

In the circular reduced three-body problem, the only first integral of motion is the Jacobi constant (Moulton 1914; Ovenden & Roy 1961),

$$C = \Phi + \frac{1}{2}(\dot{x}^2 + \dot{y}^2) = \varepsilon - h, \quad (17)$$

which is the difference between the energy and the angular momentum of the particle with respect to the observer frame. We use the Jacobi constant to determine the accuracy of our calculations.

3.1.2 Initial position and velocity

We integrate trajectories from a given initial position, \mathbf{x}_i , relative to L1 and initial velocity, \mathbf{v}_i , relative to the co-rotating frame.

The initial position is,

$$\mathbf{x}_i = \mathbf{x}_{\text{minor offset}} + \mathbf{x}_{\text{stream area offset}}. \quad (18)$$

Here $\mathbf{x}_{\text{minor offset}} = [\delta x, 0]$ is a minor offset to prevent the particle starting exactly on L1, where $\delta x = |x_{L1} - x_{\text{acc}}|/100$, x_{acc} is the position of the accretor, and x_{L1} is the x -coordinate of L1, and $\mathbf{x}_{\text{stream area offset}} = [x_{\text{stream area offset}}, 0]$ is an offset to sample the surface area of the stream at L1 (Section 2.2.2).

The initial velocity is,

$$\mathbf{v}_i = \mathbf{v}_{\text{non-synchronous offset}} + \mathbf{v}_{\text{thermal}}, \quad (19)$$

where $\mathbf{v}_{\text{thermal}} = [v_{\text{thermal}}, 0]$ is the thermal velocity of the particle in the stream (Section 2.2.1). $\mathbf{v}_{\text{asynchronous offset}} = [0, (f_{\text{sync}} - 1)d_{\text{don, L1}}]$ is the velocity relative to the co-rotating frame due to the non-synchronous rotation of the donor, and $d_{\text{don, L1}}$ is the normalised distance from the centre of the donor to L1 (Kruszewski

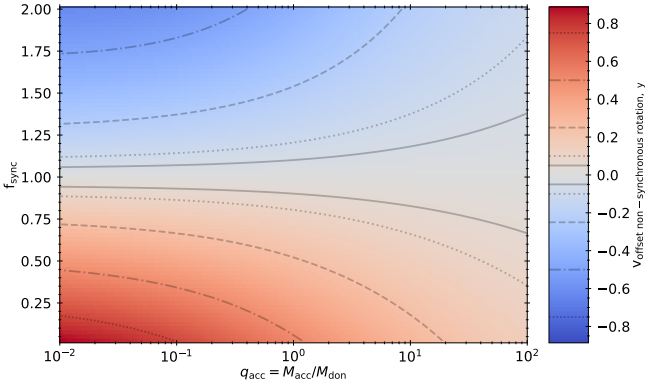


Figure 3. The y -component of the velocity offset due to non-synchronous rotation of the donor $v_{\text{non-synchronous offset}}$ as a function of q_{acc} (abscissa) and f_{sync} (ordinate). Lines of equal and opposite velocities are indicated with black transparent lines, where solid indicates 0.05 and -0.05, dotted indicates 0.1 and -0.1, dashed indicates 0.25 and -0.25, dashed-dotted indicates 0.5 and -0.5, and fine-dotted indicates 0.75 and -0.75. This figure illustrates the magnitude of the velocity due to asynchronous rotation in units of the orbital velocity. Generally, with higher mass-ratio, the lower the velocity offset due to asynchronous rotation is. This is due to the increasingly smaller size of the donor relative to the system. At low mass-ratio there is a clear asymmetry, with at low ($f_{\text{sync}} \sim 0.2$) synchronicity the velocity offset is larger in absolute terms than at high ($f_{\text{sync}} \sim 1.8$) synchronicity. This is due to that the L1 point moves outward for lower synchronicity which increases the velocity offset.

1964a). The synchronicity changes the tangential velocity offset in two ways. It determines the angular velocity offset, $f_{\text{sync}} - 1$, and it affects the distance, $d_{\text{don}, L1}$ (equation 4 and Fig. B1). We show the y -component of $v_{\text{non-synchronous offset}}$ as a function of f_{sync} and q_{acc} in Fig. 3. Generally, with higher mass-ratio, the lower the velocity offset due to asynchronous rotation is. This is due to the increasingly smaller size of the donor relative to the system. At low mass-ratio this effect is reversed, and there is a clear asymmetry, with at low ($f_{\text{sync}} \sim 0.2$) synchronicity the velocity offset is larger in absolute terms than at high ($f_{\text{sync}} \sim 1.8$) synchronicity. This is due to that the L1 point moves outward for lower synchronicity which increases the velocity offset.

We show the initial position and velocity components for an equal mass binary ($q_{\text{acc}} = 1$) with a sub-synchronously rotating donor ($f_{\text{sync}} = 0.6$) and a hot stream ($v_{\text{thermal}} = 0.1$) in Fig. 4, where the thick black and red arrows indicate the position and momentum vectors respectively, and the thin dashed lines indicate their component vectors.

3.2 Integration method

We calculate ballistic trajectories by solving the equations of motion (equations 13 and 14) with an explicit 4th order Runge-Kutta method using the `DOPRI5` ODE solver (Hairer et al. 2008) from the `PYTHON SCIPY` package (Virtanen et al. 2020). We use an adaptive method that rejects the model and halves the time step if the relative error on the Jacobi constant exceeds 10^{-6} . We either terminate the integration based on a classification of the trajectory (Section 3.3) or when the integrator fails to conserve the Jacobi constant and the time step is shorter than $10^{-20} \omega^{-1}$.

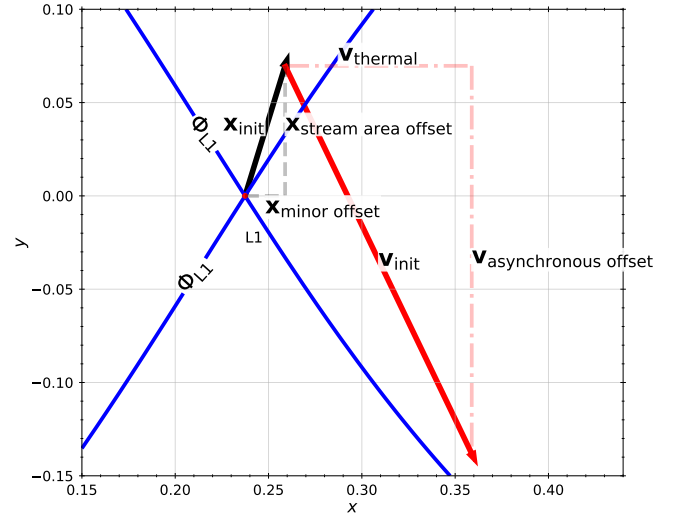


Figure 4. The initial position and initial velocity of the particle in our ballistic integrations. The solid blue line indicates the equipotential corresponding to the Roche lobe. The grey-dashed lines indicate the components of the initial position due to the mass stream sampling and the minor offset. The solid black line indicates the initial position vector relative to L1. The red-dashed lines indicate the components of the initial velocity due to thermal velocity and asynchronous rotation. The solid red line indicates the initial velocity vector relative to the rotation rate of the system. The length of the vectors is not to scale and only serves for illustration purposes, but the L1 equipotential line corresponds to a sub-synchronously rotating donor ($f_{\text{sync}} = 0.6$) in an equal mass binary ($q_{\text{acc}} = 1$) with a hot stream ($v_{\text{thermal}} = 0.1$). The position offset is enhanced for illustrative purpose.

3.3 Classifying and averaging trajectories

For each set of parameters [v_{thermal} , f_{sync} , q_{acc}] we integrate $N_{A, \text{stream}}$ trajectories, each with a position offset $x_{\text{stream area offset}, i}$ and a weighting $w_{A, \text{stream}, i}$ (Section 2.2, equation 11).

The trajectories are classified by their behaviour and outcome. Particles accrete onto either the accretor or the donor, or are lost from the system. Classification happens during integration, and changes how the calculation is terminated.

(i) **Accretion onto accretor:** Classified by motion towards the accretor, away from the donor, away from L1, into a deeper potential than L1, and within the Roche lobe of the accretor. Terminated at the moment the particle starts moving away from the accretor.

(ii) **Accretion onto donor:** Classified by motion towards the donor, away from the accretor, away from L1, into a deeper potential than L1 and within the Roche lobe of the donor. Terminated at the moment of classification.

(iii) **Lost from system:** Classified by distance from centre of mass > 3 . Terminated on classification.

We show an example of different classifications in Fig. 5

Of the trajectories that are not terminated for numerical reasons, we calculate weighted averages of their properties. We determine the fraction, β_{acc} , of our trajectories that accrete onto the accretor,

$$\beta_{\text{acc}} = \frac{\sum_{i \in C} \delta_i w_{A, \text{stream}, i}}{\sum_{i \in C} w_{A, \text{stream}, i}}, \quad (20)$$

where $w_{A, \text{stream}, i}$ is the weight of the sampled position offset along the mass stream cross-section, C is the set of classified trajectories,

and

$$\delta_i = \begin{cases} 1 & \text{if trajectory}_i \text{ classification is accretion onto accretor, and} \\ 0 & \text{otherwise.} \end{cases} \quad (21)$$

We calculate the fraction that accretes back onto the donor, β_{don} , in the same way as β_{acc} (equations 20 and 21). We calculate the fraction of trajectories that is lost from the system or classified as $\beta_{\text{lost}} = 1 - \beta_{\text{acc}} - \beta_{\text{don}}$.

We denote the total weight of all trajectories that are successfully categorised with,

$$w_{\text{successful}} = \sum_{i \in C} w_{A \text{ stream}, i}, \quad (22)$$

and the total weight of all those that fail or are rejected with,

$$w_{\text{fail}} = 1 - w_{\text{successful}}, \quad (23)$$

which can occur when our integrator is not able to conserve the Jacobi constant within the minimum time step threshold (Section 3.2).

With these weights and fractions we can quickly identify how successful our calculations are for a given set of parameters [v_{thermal} , f_{sync} , q_{acc}], and how the trajectories are classified.

3.4 Intersecting orbits

At each coordinate in our parameter space we evolve a set of trajectories sampled along the stream diameter (Section 2.2.2). We treat each of these trajectories independently, even though these trajectories can cross either themselves or each-other. To find intersecting trajectories we use the *SweepIntersectorLib*¹, which is a Python implementation of the *Sweep line algorithm* of Mehlhorn & Näher (1994). Orbits that self-intersect are always flagged as such, but only trajectories with an angle of intersection, $\theta_{\text{intersect}}$, with another trajectory larger than $\theta_{\text{threshold}} = 45^\circ$ get flagged as intersecting with others. While the exact threshold angle is not strongly motivated, we argue that low-angle intersecting trajectories would merge and be well approximated by their weighted average, high angles of intersection could significantly change the outcome of both trajectories. Fig. 5 shows the different types of intersection for a system with $q_{\text{acc}} = 10^{-1.2}$, $f_{\text{sync}} = 0.22$, and $v_{\text{thermal}} = 10^{-0.5}$, and $N_{A, \text{stream}} = 12$ equally spaced sampled trajectories. At each coordinate we record the weighted fraction of trajectories that self-intersect, $f_{\text{self intersect}}$, as well as those that intersect with other trajectories, $f_{\text{other intersect}}$, if their intersection angle exceeds the threshold.

3.5 Radii, specific angular momenta and torques

When the mass stream misses the accretor it loops back around and form an accretion disk. This disk forms at the circularisation radius, defined as the radius where the specific angular momentum, $h_{\text{stream, min, acc}}$, with respect to the accretor at the moment of closest approach, r_{min} , equals that of a circular Keplerian orbit around the accretor with radius

$$r_{\text{circ}} = \frac{h_{\text{stream, min, acc}}^2}{\mu_{\text{acc}}}. \quad (24)$$

¹ https://github.com/prochitecture/sweep_intersector

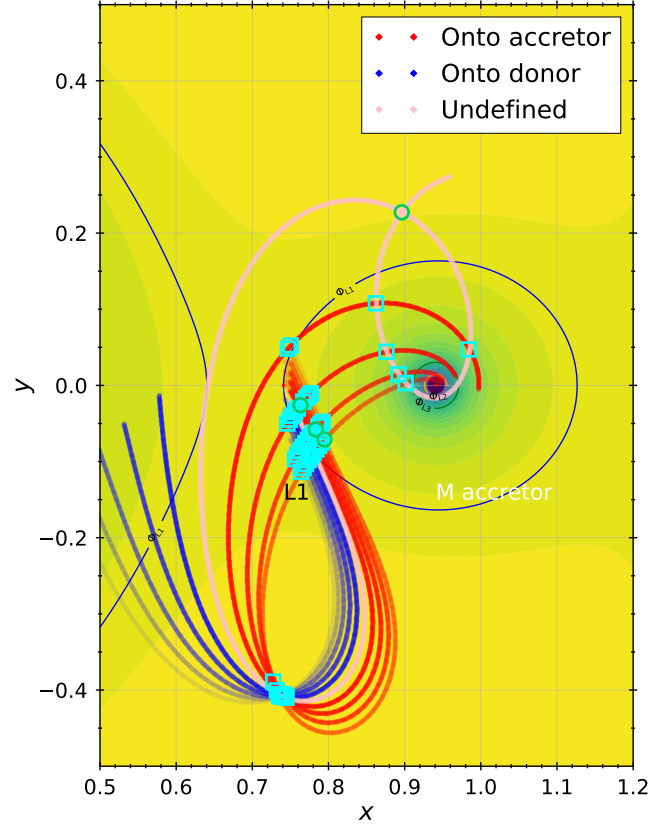


Figure 5. Trajectories for $q_{\text{acc}} = 10^{-1.2}$, $f_{\text{sync}} = 0.22$, and $v_{\text{thermal}} = 10^{-0.5}$, and $N_{A, \text{stream}} = 12$ equally spaced sampled trajectories around the mass transfer stream centre. The red trajectories are classified as accreting onto the accretor. The dark-blue trajectories are classified as accreting back onto the donor. The green circles are locations of self-intersection and the light-blue squares are locations of intersection with other trajectories. This illustrates the different trajectory classes as well as the intersections that occur between the trajectories.

The specific angular momentum of a particle with respect to the accretor is,

$$\begin{aligned} h_{\text{acc}} &= (x - x_{\text{acc}})^2 + (y - y_{\text{acc}})^2 + (x - x_{\text{don}})\dot{y} - \dot{x}(y - y_{\text{don}}), \\ &= (x - 1 + \mu_{\text{acc}})^2 + y^2 + (x - 1 + \mu_{\text{acc}})\dot{y} - \dot{x}y. \end{aligned} \quad (25)$$

We calculate $h_{\text{stream, min, acc}}$ by evaluating equation 25 at the radius of closest approach.

While in our ballistic trajectory calculations we implicitly assume that the stream will miss the accretor and will form an accretion disk around the star, many interacting binaries actually transfer mass through direct-impact accretion. When the stream collides with the accretor, i.e. direct-impact accretion $r_{\text{stream}} < r_{\text{accretor}}$, the specific angular momentum of the stream (equation 25) at that point is different than at the point of closest approach during disk formation. We calculate the specific angular momentum of the stream with respect to the accretor as a function of the distance to the centre of the accretor. This allows a more accurate determination of the specific angular momentum accretion rate when the stream directly impacts the accretor. We record the (averaged) specific angular momentum of the stream at fixed distances from the accretor, with a minimum distance of $d_{\text{stream min}}$, a maximum distance of $d_{\text{stream max}}$ at N_{radii}

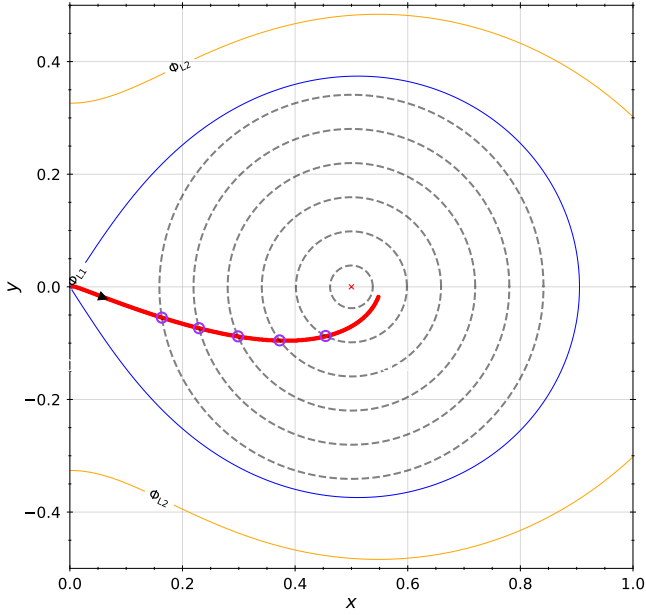


Figure 6. Locations at which we record the specific angular momentum of the stream along the stream trajectory. The solid blue line indicates the equipotential surface coinciding with L1 (i.e. Roche-Lobe). The solid orange line indicates the equipotential surface coinciding with L2. The solid red line indicates the stream trajectory. The dashed grey lines indicates equidistant lines from the centre of mass of the accretor. The purple circles indicate the intersection point of the stream with the equidistant. The black arrow indicates the direction of travel of the stream. The number and radii of the equidistances are chosen to illustrate the situation, but may differ in our datasets. We record the specific angular momentum along the stream to determine the torque on the accretor in the case of direct-impact accretion.

equally spaced radii, located at,

$$d_{\text{stream } i} = d_{\text{stream min}} + i \times \frac{(d_{\text{stream max}} - d_{\text{stream min}})}{N_{\text{radii}}}. \quad (26)$$

Here $d_{\text{stream } i}$ indicates the i -th radius from the centre of the accretor in units of the Roche-lobe radius of the accretor, at which we record the i -th specific angular momentum along the stream $h_{\text{stream } i}$. We show a schematic example of the locations at which we record the specific angular momentum of the stream in Fig. 6.

3.5.1 Self-accretion torque

Accretion of (part of) the mass transfer stream back onto the donor exerts a torque on the donor star. We calculate the specific angular momentum of a particle at the moment of impact on the donor, with respect to the donor,

$$\begin{aligned} h_{\text{don}} &= (x - x_{\text{don}})^2 + (y - y_{\text{don}})^2 + (x - x_{\text{don}})\dot{y} - \dot{x}(y - y_{\text{don}}), \\ &= (x + \mu_{\text{acc}})^2 + y^2 + (x + \mu_{\text{acc}})\dot{y} - \dot{x}y. \end{aligned} \quad (27)$$

We calculate the initial $h_{i, \text{don}}$ and final $h_{f, \text{don}}$ specific angular momentum of a particle accreting back onto the donor by evaluating equation 27 with the initial and final positions and velocities respectively, and we use these specific angular momenta to calculate the total torque on the donor due to self-accretion.

3.6 Properties of mass transfer in binary populations

To inform us of the ranges of q_{acc} , f_{sync} and v_{thermal} we should cover, we evolve a binary population with the rapid binary population synthesis framework BINARY_C (Izzard et al. 2004, 2006, 2009, 2018; Izzard & Jermyn 2022; Hendriks & Izzard 2023), which is based on the algorithm from Hurley et al. (2000, 2002), and makes use of the single star models of Pols et al. (1998) and provides analytical fits to their evolution as in Tout et al. (1997). Specifically relevant to this study are the tidal interactions between binary stars. These are implemented as in Hurley et al. (2002), in which dynamical tides are based on (Zahn 1975, 1977a) and equilibrium tides are based on Hut (1981).

Our population contains binary systems with an initial primary mass M_1 , secondary mass M_2 and orbital period P , and we assign weights to each system according to the distribution functions of their birth properties of Moe & Stefano (2017). M_1 is sampled logarithmically in the range 0.8 to 120 M_{\odot} . M_2 is sampled from a flat mass-ratio distribution between $0.1M_{\odot}/M_1$ and 1. P is sampled from a logarithmically-spaced distribution of periods between 1 day and 10^8 days. We evolve $N_{M_1} \times N_{M_2} \times N_P = 80 \times 80 \times 80$ binary systems sampled with the distributions described above at near-solar metallicity ($Z = 0.02$).

During Roche-lobe overflow we record the mass transfer quantities v_{thermal} , f_{sync} and q_{acc} , and we weigh them by the time spent transferring mass and the mass transferred,

$$\begin{aligned} W_{\text{time}, i} &= p_i * dt \text{ [yr]} \\ W_{\text{mass}, i} &= p_i * dt \dot{M}_{\text{don}} [M_{\odot}], \end{aligned} \quad (28)$$

where $W_{\text{time}, i}$ is the time-weighted probability, $W_{\text{mass}, i}$ is the mass-weighted probability, p_i is the probability of the i -th system according to the distribution functions of Moe & Stefano (2017) dt is the time-step taken in BINARY_C and \dot{M}_{don} is the mass-transfer rate of the donor.

Based on our results of our binary population, we determine the parameter ranges for our ballistic interpolation calculations (Table 1). We use these ranges to span a hypercube of initial parameters for our ballistic calculations.

4 RESULTS

We present our results in the following sections. First, we show our binary population which contain data on the properties of the mass transfer in many systems. We then take these results and use them to determine the ranges of the parameters in our trajectory calculations. We then show our ballistic trajectory results for “cold” (narrow and slow) and “hot” (wide and fast) streams.

4.1 Mass transfer in binary populations

With the results of our stellar population generated in Section 3.6, we calculate the ranges of the parameters of interest in a population of interacting binary systems. Our results include the average time spent, and the average mass transferred, of each system configuration.

Fig. 7 shows the distributions of the parameters of interest, weighted either by time spent transferring mass or mass transferred. We normalise the area under each of the curves to unity, and we define values $< 10^{-5}$ as rare and indicate them by a green horizontal line.

Fig. 7 (a) shows the logarithmic thermal-velocity, $\log_{10}(v_{\text{thermal}})$, distributions. All systems have thermal-velocities between $10^{-3.5}$

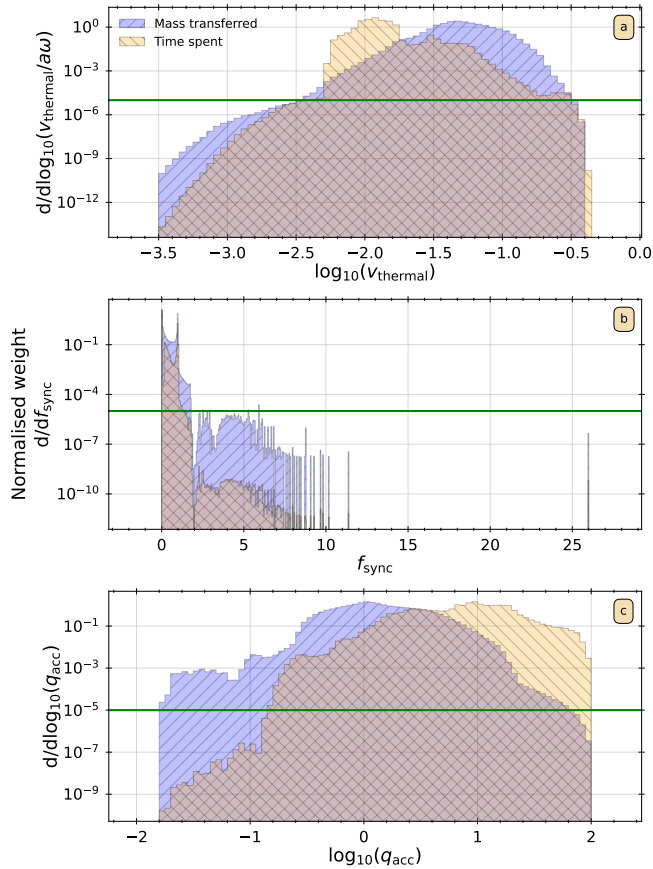


Figure 7. Parameter distributions obtained from our binary stellar population simulations (Section 3.6). (a) shows the thermal-velocity $\log_{10}(v_{\text{thermal}})$, (b) shows the synchronicity factor f_{sync} and (c) shows the mass ratio $\log_{10}(q_{\text{acc}})$. The blue hatched areas show the mass-weighted distribution of each parameter, and the orange hatched areas show the time-weighted distribution. The green horizontal line indicates the weighted probability density of 10^{-5} .

and $10^{-0.5}$. Fig. 7 (b) shows the synchronicity fraction, f_{sync} , distributions. These are mostly between 0 and 2, with a peak around both 0 and 1 for both the time spent transferring mass and mass-transferred weights. While the time-spent distribution peaks at synchronous rotation rates ($f_{\text{sync}} = 1$), the mass-transferred distribution peaks at very sub-synchronous rotation rates ($f_{\text{sync}} \sim 0$). There is a large tail of synchronicity fractions from $f_{\text{sync}} = 2$ to $f_{\text{sync}} \approx 10$, but their probability is low. Fig. 7 (c) shows the mass ratio, $\log_{10}(q_{\text{acc}})$, distribution. We see a single main range between $\log_{10}(q_{\text{acc}}) = -2$ and 2 for both the time spent and mass transferred weights. The data show that at small mass ratios ($q_{\text{acc}} < 1$) hardly any time is spent transferring mass (probabilities up to 10^{-4}), while at larger mass ratios ($q_{\text{acc}} > 1$) the opposite is true. This is understood by the mass ratio reversal during mass transfer and the transition from thermal timescale mass transfer (high mass-transfer rate, short time) to nuclear timescale mass transfer (low mass-transfer rate, long time).

We show the distributions of the logarithm of the ratio of the dynamical timescale of the donor to the tidal timescale, $\log_{10}(\eta_{\text{static}})$ in Fig. 8. We indicate equal-valued timescales, $\log_{10}(\eta_{\text{static}}) = 0$ with a red-dashed vertical line. The area on the right of this line indicates that the static-tide approximation is justified, and vice versa. The numbers in the legend indicate the total fraction for either weights with $\log_{10}(\eta_{\text{static}}) < 0$. The data show a broad range of

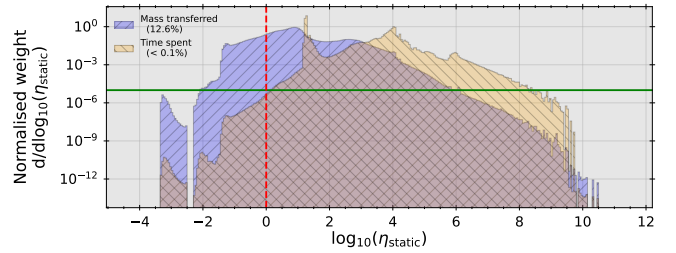


Figure 8. Normalised weighted distribution of $\log_{10}(\eta_{\text{static}})$, the quantity that captures the validity of the static tides approximation (equations 5 and 6). Blue indicates weighted by mass-transferred, orange indicates weighted by time-spent transferring mass (equation 28). The regions where both histograms overlap are coloured darker red. The green horizontal line indicates the normalised weight of 10^{-5} and the red-dashed vertical line indicates $\log_{10}(\eta_{\text{static}}) = 0$, above which the tides induced by the non-synchronous rotation are approximately static. The legend includes the fraction of the total weighted mass-transferred or time-spent with $\log_{10}(\eta_{\text{static}}) < 0$.

$\log_{10}(\eta_{\text{static}})$, and clearly show that in terms of time-spent transferring mass, the static approximation is overall valid (less than 0.1 per cent below $\log_{10}(\eta_{\text{static}}) = 0$). This is not always the case for the mass-transferred, because a significant fraction (13 per cent) of all mass transferred occurs when the static-tide approximation is invalid.

We show the normalised distribution of $\log_{10}(\eta_{\text{static}})$ as a function of f_{sync} in Fig. 9, where in Fig. 9 (a) we show the distribution weighted by mass-transferred, and in Fig. 9 (b) we show the data in terms of time-spent transferring mass. We indicate 6 sections, separated by red-dotted lines. Section I indicates super-synchronous ($f_{\text{sync}} > 1.025$) systems where the potential is approximately static ($\log_{10}(\eta_{\text{static}}) \geq 0$), section II indicates near-synchronous systems ($0.975 \leq f_{\text{sync}} \leq 1.025$) with a static potential ($\log_{10}(\eta_{\text{static}}) \geq 0$) and section III indicates sub-synchronous systems ($0.975 < f_{\text{sync}} < 1.025$) with a static potential ($\log_{10}(\eta_{\text{static}}) \geq 0$). Section IV indicates sub-synchronous systems ($0.975 < f_{\text{sync}} < 1.025$) where the static approximation is not valid ($\log_{10}(\eta_{\text{static}}) < 0$, i.e. with a dynamic potential), section V indicates near-synchronous systems ($0.975 \leq f_{\text{sync}} \leq 1.025$) with a dynamic potential ($\log_{10}(\eta_{\text{static}}) < 0$) and section VI indicates super-synchronous systems ($f_{\text{sync}} > 1.025$) with a dynamic potential ($\log_{10}(\eta_{\text{static}}) < 0$). The range of f_{sync} in the near-synchronous regions is determined by the bin-width in our simulations. Fig. 9 (a) shows that the transferred mass is mostly transferred in three sections. Only 9.8 per cent of the systems normalised by mass-transferred are synchronous and are well approximated by the static potential (section II). The large majority (77.5 per cent) of transferred mass takes place in systems with a sub-synchronous donor that still responds rapidly enough to regard the potential as static (section III). Most of the remaining systems (12.6 per cent) have donors that rotate sub-synchronously for which the static potential approximation does not hold (section IV). The rest of the sections cover less than 0.08 per cent of all transferred mass, which indicates that super-synchronous rotation does not occur much in field binaries (< 0.07 per cent), and especially not in cases where the static potential approximation breaks down. Fig. 9 (b) shows that the time-spent transferring mass mostly is spent in just two sections, section II and III. Between these two sections, the synchronous case where the static potential approximation holds (section II) covers 37.6 per cent of all time-spent transferring mass. The majority, thus, is spent where systems have donors that rotate sub-synchronously but effectively experience a static potential. The contribution of the other regions is negligible

(< 0.04), indicating that like in the mass-transferred case super-synchronous rotation is not common in field binaries, but also that not much time is spent in the case where the donor effectively experiences dynamical tides.

With our results shown in Fig. 7 and Fig. 9 we determine the parameter ranges for the trajectory simulations.

(i) For the thermal velocity, $\log_{10}(v_{\text{thermal}})$, we consider the range between -3.5 and -0.5 for our trajectory calculations.

(ii) For the synchronicity factor, f_{sync} , we consider the range between 0 and 2 for our trajectory calculations. A small fraction of systems has $f_{\text{sync}} > 2$, they are however clearly less frequent.

(iii) For the mass ratio, q_{acc} , we use the range between -2 and 2 for our trajectory calculations.

These values are listed in Table 1.

The above results indicate that sub-synchronous mass-transfer is common, both for the time-spent (> 60 per cent) and for the mass-transferred (90 per cent). This further motivates the remainder of this study.

4.2 Ballistic trajectory properties

In this section we show our results of the ballistic trajectory calculations. While our results span a large parameter space, we choose to highlight the two extreme cases, with the results for cold and narrow streams ($v_{\text{thermal}} = 10^{-3}$ and $D_{\text{stream}} \approx 10^{-4} - 10^{-3}$) in Section 4.2.1 and hot and wide streams ($v_{\text{thermal}} = 10^{-0.5}$ and $D_{\text{stream}} \approx 0.1 - 0.4$) in Section 4.2.2. Before looking at the results let us highlight several effects that are relevant to the evolution of the trajectories.

In sub-synchronous systems ($f_{\text{sync}} < 1$) L1 moves outward relative to the synchronous case, the velocity offset due to asynchronous rotation at L1 is downward ($v_{\text{non-synchronous offset}}$ is negative), the Coriolis force for downward motion leads to a rightward acceleration ($a_{\text{Coriolis, y}}$ is positive), and at the moment of release the particle is located within the Roche lobe of the accretor. In super-synchronous systems ($f_{\text{sync}} > 1$) L1 moves inward relative to the synchronous case, the velocity offset due to asynchronous rotation at L1 is upward ($v_{\text{non-synchronous offset}}$ is positive), the Coriolis force for upward motion leads to a leftward acceleration ($a_{\text{Coriolis, y}}$ is negative) and at the moment of release the particle is located within the Roche lobe of the donor. In low mass ratio systems ($q_{\text{acc}} < 1$) the velocity offset due to asynchronous rotation is larger relative to equal mass-ratio systems due to the large size of the Roche-lobe of the donor and the velocity is even higher for sub-synchronous rotation as L1 moves outward. In high mass ratio systems ($q_{\text{acc}} > 1$) the velocity offset due to asynchronous rotation is smaller relative to the equal mass-ratio systems due to the small size of the Roche-lobe of the donor. These effects are visualised and quantified in Figures 2, 3 and B1, and equation 13.

4.2.1 Cold and narrow streams

We show our cold and narrow ballistic integrations, $v_{\text{thermal}} = 10^{-3}$, in the ranges of mass ratio, q_{acc} , and synchronicity factor, f_{sync} , described in Table 1. From Fig. 2 we know that the stream diameter is small, $D_{\text{stream}} \approx 10^{-4} - 10^{-3}$, so all the trajectories sampled along the stream effectively have the same initial position. From Fig. 3 we know that for asynchronous systems ($f_{\text{sync}} \neq 1$) at low mass ratios $q_{\text{acc}} < 1$ the initial radial velocity is low compared to the tangential asynchronous velocity offset, $v_{\text{asynchronous offset}}$, which indicates that results in that part of the parameter space will deviate most from the synchronous case explored by (Lubow & Shu 1975).

In Fig. 10 we show the radii of closest approach, r_{min} , of particles that accrete onto the accretor as a function of mass ratio, q_{acc} (abscissa), and donor synchronicity, f_{sync} (colour scale). The triangles indicate the orientation of the particle, where the upward triangle indicates prograde (same direction as the binary orbit) orientation and the downward triangle indicates retrograde (opposite direction). The red diamonds are from Lubow & Shu (1975), and the blue dashed line indicates the prescription of Ulrich & Burger (1976). The radii of closest approach in synchronously-rotating $f_{\text{sync}} = 1$ donor systems match closely to the results of Lubow & Shu (1975).

Overall, in the range that covers the parameters of Lubow & Shu (1975, $8 \times 10^{-2} < q_{\text{acc}} < 2 \times 10^1$ and $f_{\text{sync}} = 1$) we find a good match, confirming that our method works as it should, given the assumptions and approach. Our data show the super-synchronous donors only accrete onto the accretor at high mass ratios ($q_{\text{acc}} > 10$ and $f_{\text{sync}} > 1.5$), with a decrease in minimum q_{acc} required for accretion onto the donor with a decrease in f_{sync} . At high mass-ratio the donor is not able to exert enough force to turn the stream back onto itself even though the particle is released within its Roche-Lobe, due to its low mass. With sub-synchronous donors we find an increase in the minimum mass-ratio that accretes onto the accretor, with decreasing f_{sync} . Moreover, given a synchronicity factor, f_{sync} , the radius of closest approach decreases with decreasing mass ratio, q_{acc} . Systems with a low mass ratio and a low synchronicity factor ($q_{\text{acc}} < 1$ and $f_{\text{sync}} < 0.4$) experience a high negative velocity offset due to asynchronous rotation and, even though they initially start in the Roche lobe of the accretor, they experience an acceleration towards the donor because of the Coriolis force, which is strong enough to steer the trajectory onto the donor. Generally, in high mass-ratio systems, the effect of asynchronous rotation on the radius of closest approach is small, with a spread of only a factor of 2 at $q_{\text{acc}} \sim 30$. This is because the velocity offset due to the asynchronous rotation for systems with mass-ratio $q_{\text{acc}} \geq 30$ is generally low ($|v_{\text{asynchronous offset}}| < 0.2$, Fig. 3), so the trajectories do not differ much from the synchronous case.

In Fig. 11 we show the ratio of circularisation radius to radius of closest approach, $r_{\text{circ}}/r_{\text{min}}$, as a function of mass ratio, q_{acc} , and synchronicity factor, f_{sync} . This data is a measure of the specific angular momentum at the radius of closest approach and how much it differs from that of a circular orbit at the radius of closest approach. Moreover, this data is used to calculate the radius at which an accretion disk forms. The red diamonds are from Lubow & Shu (1975) and the blue-dashed horizontal line is from Ulrich & Burger (1976). At high mass-ratios ($q_{\text{acc}} > 10$), we see a general decrease of the $r_{\text{circ}}/r_{\text{min}}$ with increasing mass ratio q_{acc} , regardless of the synchronicity factor, with a spread of at most 0.2. This indicates that the specific angular momentum at the radius of closest approach tends to that of a circular orbit at the radius of closest approach, and that the asynchronous rotation of the donor does not affect this quantity strongly either.

At mass-ratios $q_{\text{acc}} < 1$ the trajectories of most asynchronous donors accrete onto the accretor. All the trajectories have a ratio of radii between 1.7 and 2.0, indicating that the stream carries much more specific angular momentum at the radius of closest approach than a circular orbit would. Because of its low mass, the torque exerted by the accretor is insufficient to circularise the stream.

Overall, the ratio is between 1.3 and 2, indicating that the stream always carries more specific angular momentum than a circular orbit at the radius of closest approach would. Moreover, the commonly used constant ratio 1.7 used by Ulrich & Burger (1976) is up to 30 per cent off.

In Fig. 12 we show the fractional difference between the final

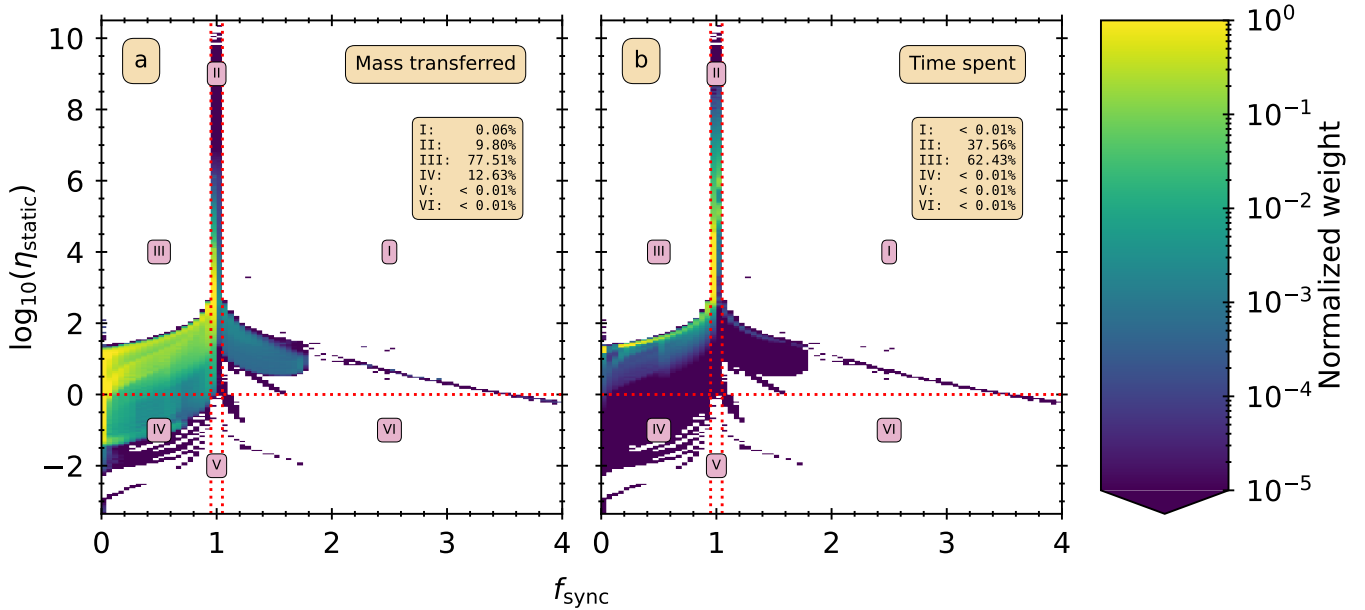


Figure 9. $\log_{10}(\eta_{\text{static}})$ (ordinate) as a function of f_{sync} (abscissa) in binary population (Section 3.6). (a) shows the distribution of $\log_{10}(\eta_{\text{static}})$ vs. f_{sync} in a population of binaries in terms of mass transferred, and (b) shows the distribution in terms of time spent transferring mass. We indicate 6 sections, separated by red-dotted lines. Section I indicates super-synchronous ($f_{\text{sync}} > 1.025$) systems where the potential is approximately static ($\log_{10}(\eta_{\text{static}}) \geq 0$), section II indicates near-synchronous systems ($0.975 \leq f_{\text{sync}} \leq 1.025$) with a static potential ($\log_{10}(\eta_{\text{static}}) \geq 0$) and section III indicates sub-synchronous systems ($0.975 < f_{\text{sync}}$) with a static potential ($\log_{10}(\eta_{\text{static}}) \geq 0$). Section IV indicates sub-synchronous systems ($0.975 < f_{\text{sync}}$) where the static approximation is not valid ($\log_{10}(\eta_{\text{static}}) < 0$, i.e. with a dynamic potential), section V indicates near-synchronous systems ($0.975 \leq f_{\text{sync}} \leq 1.025$) with a dynamic potential ($\log_{10}(\eta_{\text{static}}) < 0$) and section VI indicates super-synchronous systems ($f_{\text{sync}} > 1.025$) with a dynamic potential ($\log_{10}(\eta_{\text{static}}) < 0$). The range of f_{sync} in the near-synchronous regions is determined by the bin-width in our simulations.

Parameter	[lower bound, upper bound, step size]	comment
$\log_{10}(v_{\text{thermal}})$	[-3.5, -0.5, 0.5]	thermal velocity (Section 2.2.1 and equation 7).
f_{sync}	[0.1, 2.0, 0.1]	Synchronicity factor (Section 2.1 and equation 3).
$\log_{10}(q_{\text{acc}})$	[-2, 2, 0.1]	Mass ratio $q_{\text{acc}} = M_{\text{acc}}/M_{\text{don}}$.

Table 1. Parameters and ranges used to generate our interpolation dataset. The first column describes the parameter, the second column describes the parameter range and step size, and the third column contains extra descriptions and references to the appropriate formulae.

($h_{f, \text{don}}$) and initial ($h_{i, \text{don}}$) specific angular momenta (ordinate) of particles that accrete back onto the donor as a function of mass ratio, q_{acc} (abscissa), and synchronicity fraction, f_{sync} . The data show two distinct regions.

The trajectories from sub-synchronous donors ($f_{\text{sync}} \leq 0.7$) show an increasingly larger final specific angular momentum $h_{f, \text{don}}$ compared to the initial specific angular momentum, $h_{i, \text{don}}$, of the stream for decreasing synchronicity factor, f_{sync} . Moreover, the lower f_{sync} , the larger the range in mass-ratios, q_{acc} , for which the stream accretes onto the donor. This is because a larger deviation from synchronism introduces a larger velocity offset, which requires an increasingly massive accretor to completely turn the stream towards itself. These trajectories all exert a positive torque on the donor that leads to the donor becoming more synchronous.

Trajectories from super-synchronous donors show a decrease in specific angular momentum relative to their initial specific angular momentum, with a decrease in specific angular momentum relative to the initial angular momentum as f_{sync} increases. This is because of a decrease in angle of incidence with the donor with increasing asynchronicity for super-synchronous donors, caused by a combination of a lower velocity offset and an acceleration towards the donor,

and vice versa for sub-synchronous donors. Trajectories that accrete onto super-synchronous donors all exert a negative torque that again leads to the donor becoming more synchronous.

For both the super-synchronous (negative torque) and the sub-synchronous (positive torque) torque self-accretion, the magnitude of the difference between the initial and final specific angular momenta increases, for a given synchronicity factor, with increasing mass ratio q_{acc} . At higher mass-ratios the trajectory is affected more, due to the stronger gravitational effect of the accretor. This increasingly affects the final angular momentum of the stream, which leads to the increasing difference. In the low mass-ratio systems, the stream angular momentum is hardly affected, and thus the difference remains small (e.g. at $q_{\text{acc}} = 0.01$, $h_{f, \text{don}}/h_{i, \text{don}} - 1 > -10^{-1}$ for sub-synchronous donors, and $h_{f, \text{don}}/h_{i, \text{don}} - 1 < 5 \times 10^{-1}$ for super-synchronous donors).

We show the fractions of each classification as a function of mass ratio, q_{acc} (abscissa), and synchronicity factor, f_{sync} (ordinate, Section 3.3, equation 20), in Fig. 13. Fig. 13 (a) shows the fraction of all trajectories accreting onto the accretor, Fig. 13 (b) shows those accreting onto the donor and Fig. 13 (c) shows those that are lost from the system. The colour-scale indicates a non-zero fraction, where a

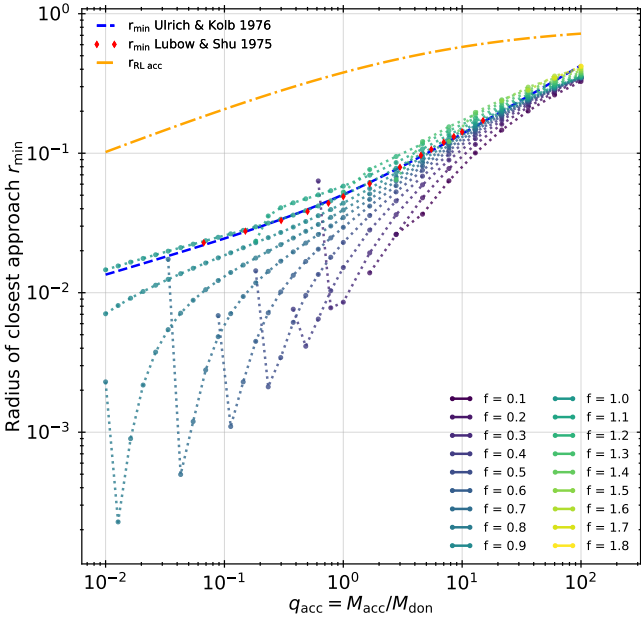


Figure 10. Radius of closest approach r_{\min} (ordinate) from our cold, $v_{\text{thermal}} = 10^{-3}$, ballistic calculations and prescriptions in the literature as a function of mass-ratio, q_{acc} (abscissa), and synchronicity factor, f_{sync} (colour-scale). The red diamonds indicate the original data points from Lubow & Shu (1975), the blue dashed line indicates the prescription from Ulrich & Burger (1976) and the orange dashed-dotted line indicates the Roche-lobe radius of the accretor.

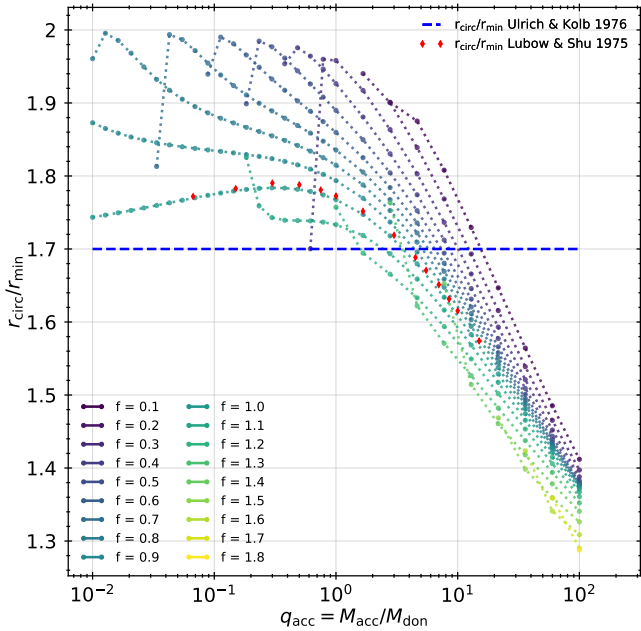


Figure 11. Ratio of circularisation radius to radius of closest approach r_{circ}/r_{\min} (ordinate) as a function of mass ratio q_{acc} (abscissa) and synchronicity factor f_{sync} (colour-scale). The red-dashed horizontal line indicates the ratio r_{circ}/r_{\min} from Ulrich & Burger (1976)

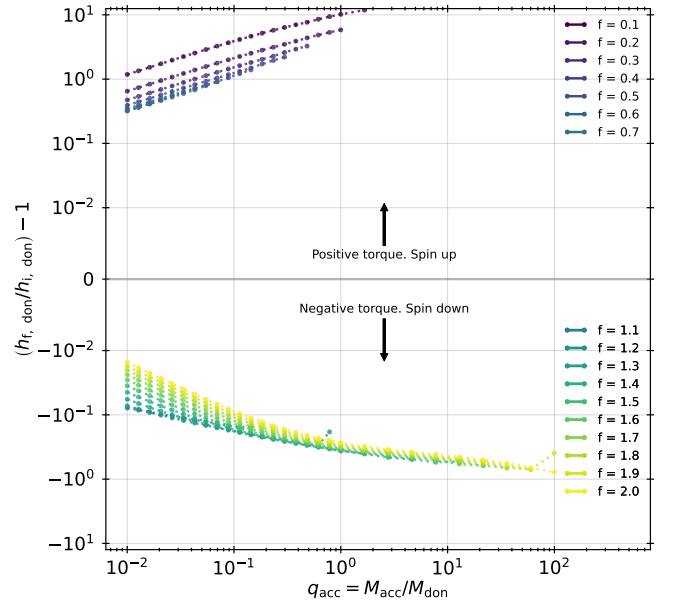


Figure 12. Fractional difference between the final ($h_{f, \text{don}}$) and initial ($h_{i, \text{don}}$) specific angular momenta (ordinate) of particles that accrete back onto the donor as a function of mass ratio q_{acc} (abscissa) and synchronicity fraction f_{sync} (colour scale). The set of values at the top originates from sub-synchronously rotating donors. The set of values at the bottom originates from super-synchronously rotating donors.

white indicates a fraction of zero. The red lines indicate the fraction of all trajectories that failed to evolve correctly (Section 3.2 and equation 23).

The data in Fig. 13 (a) show that, at low mass-ratio, ($q_{\text{acc}} < 0.1$), only the near-synchronous donors accrete onto the accretor. The region of synchronicity factor, f_{sync} , that corresponds to accretion onto the accretor increases both to sub- and super-synchronous donors with increasing mass ratio q_{acc} . This is due to the decrease in velocity offset due to asynchronous rotation with increasing q_{acc} (Fig. 3). This reduces the effect of asynchronous rotation and makes the trajectories behave like ones from synchronous systems. The asymmetry in the shape of the fraction accreted onto the accretor is caused by the Coriolis force, which accelerates the particle towards the accretor for sub-synchronous donors and away for super-synchronous donors. The data in Fig. 13 (b) show an exact inversion of the data in Fig. 13 (a), and Fig. 13 (c) shows that for the low thermal-velocity (cold) there are no trajectories that escape the system.

The transition between each region is sharp, caused by the narrow stream associated with the low thermal-velocity (cold), which indicates that for every classification at a given coordinate either none (white) of the trajectories or all (yellow) of the trajectories are classified as such. Moreover, we find no failing systems for our cold and narrow trajectories.

Fig. 14 shows the fractions of trajectory intersections (Section 3.4) as a function of q_{acc} and f_{sync} , for low thermal-velocity (cold, $v_{\text{thermal}} = 10^{-3}$) streams. The red contours show the fraction of self-intersecting trajectories, the blue contours show the fraction of intersection with other trajectories. The dashed line indicates a weighted fraction of at least 0.1 of all the trajectories, a dotted line indicates a weighted fraction of at least 0.5 and the solid line indicates a weighted fraction of at least 0.9 of all trajectories.

We find that self-intersecting orbits occur at the edges of the tran-

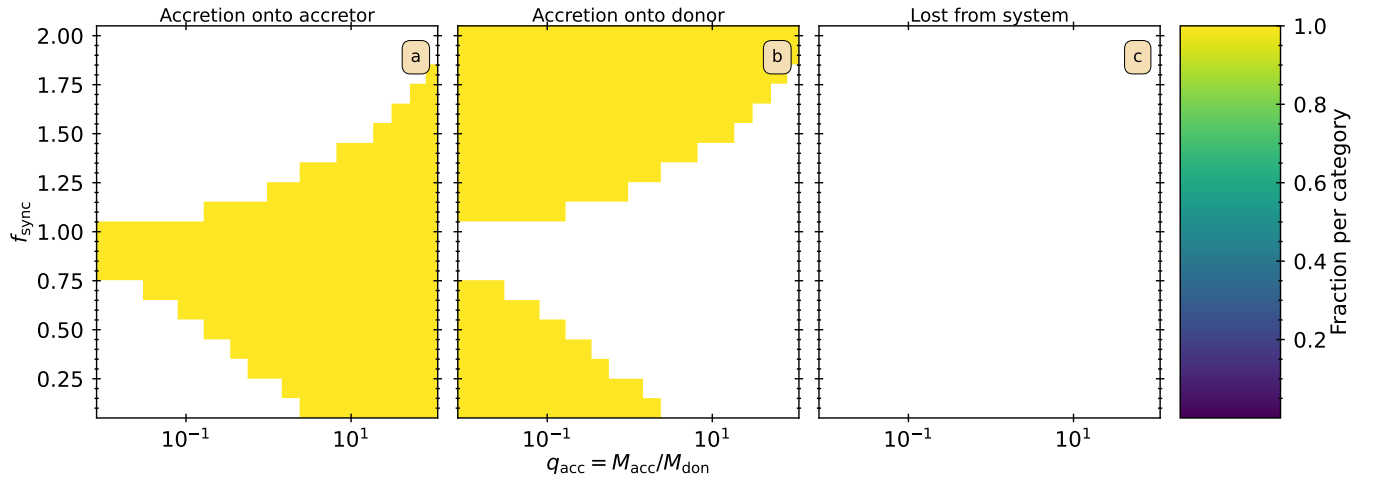


Figure 13. Fractions of trajectory classifications as a function of mass ratio q_{acc} (abscissa) and synchronicity factor f_{sync} (ordinate, Section 3.3, equation 20). (a) shows the fraction of trajectories accreting onto the accretor, (b) shows the fraction of trajectories accreting back onto the donor and (c) shows the trajectories that escape the system. Colour indicates the fraction of each classification to all the classified trajectories. White indicates a fraction of zero. The red lines indicate the fraction of all trajectories that failed to evolve correctly (Section 3.2 and equation 23).

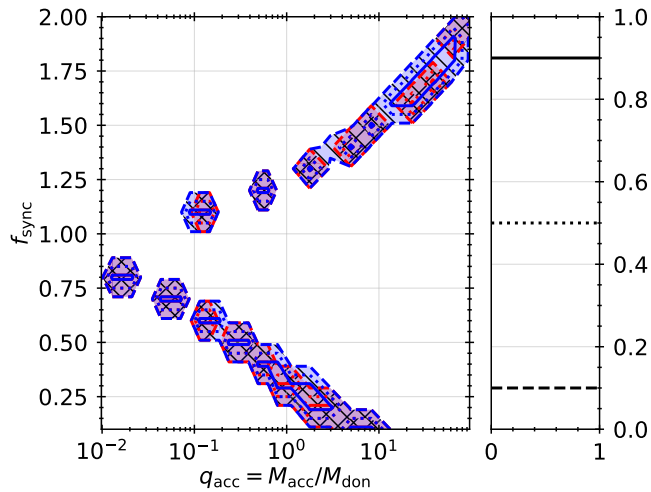


Figure 14. Fractions of trajectory intersections (Section 3.4) as a function of q_{acc} (abscissa) and synchronicity factor f_{sync} (ordinate). The red contours show the fraction of self-intersecting trajectories, $f_{\text{self intersect}}$, the blue contours show the fraction of intersection with other trajectories, $f_{\text{other intersect}}$. The dashed line indicates a weighted fraction of at least 0.1 of all the trajectories, a dotted line indicates a weighted fraction of at least 0.5 and the solid line indicates a weighted fraction of at least 0.9 of all trajectories.

sition regions between accretion onto the accretor and accretion onto the donor (Fig. 13). The fraction is always high, since the stream is itself so narrow that the trajectories stay bundled and follow approximately the same path. Intersection with other trajectories, with angles of incidence above the threshold $\theta_{\text{threshold}}$, occurs in the same narrow region of $(q_{\text{acc}}, f_{\text{sync}})$ parameter space as the self-intersecting orbits. This is because the stream is so narrow that the trajectories effectively follow the same path as each other.

In Fig. 10 and Fig. 11 we focus on properties of the stream at its radius of closest approach to the accretor. In many situations, though, the radius of the accretor exceeds the radius of closest approach and the stream directly impacts the accretor. In that case, the stream has

less travel time through the potential and experiences less torque by the binary system, which affects the specific angular momentum of the stream upon impact with the accretor. We show the evolution of the specific angular momentum of the mass-transfer stream as a function of its distance to the accretor and the mass ratio q_{acc} for systems with synchronously rotating donors ($f_{\text{sync}} = 1$) in Fig. 15. The color indicates the specific angular momentum of the stream in units of that of the specific angular momentum at the radius of closest approach. The orange lines show 5 equally spaced lines where this specific angular momentum is constant. For all mass ratios the specific angular momentum of the stream starts out higher than what the specific angular momentum at the radius of closest approach is. For systems with high mass ratios the difference between the initial specific angular momentum and that at r_{min} is minor (a few percent), but this difference increases with decreasing mass ratio (up to ten percent). We note that the qualitative behaviour of the stream systems with a different synchronicity factor, f_{sync} , and thermal velocity, v_{thermal} , is not necessarily the same as described above.

4.2.2 Hot and wide streams

In this section we show the trajectory properties of systems with a hot and wide stream ($v_{\text{thermal}} = 10^{-0.5}$ and $D_{\text{stream}} \approx 0.1 - 0.4$). Whereas in the low thermal-velocity (cold) regime the stream area is negligible, here the stream area is sufficiently large as to cause a relevant offset between the initial positions of the particles. Moreover, the high thermal-velocity (hot) provides a large initial radial velocity towards the accretor, and the Coriolis force subsequently provides a large downward (negative y-direction) acceleration on the particles.

We show the radii of closest approach in our high thermal-velocity (hot) calculations in Fig. 16. Overall, we again find a small spread of radii ($r_{\text{min}} \sim 0.3 - 0.5$) at large mass-ratios $q_{\text{acc}} = 100$, but we now see a much larger spread ($r_{\text{min}} \sim 0.01 - 0.8$) at low mass ratios ($q_{\text{acc}} \sim 0.1$). Notably, a wider range ($f_{\text{sync}} = 0.1 - 2.0$) of initial asynchronicities lead to the accretion onto the accretor. This is due to the larger ($v_{\text{thermal}} \approx 0.32$) initial radial velocity that makes it harder to deflect the stream.

Accretion onto the donor now only occurs for systems with a low

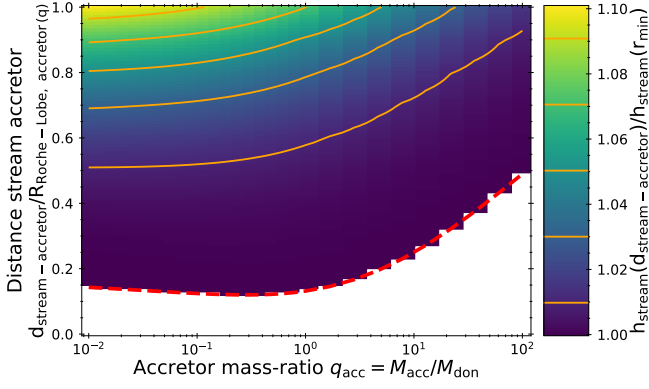


Figure 15. Specific angular momentum of the mass-transfer stream in terms of the specific angular momentum at the radius of closest approach (colour-scale) as a function of mass ratio q_{acc} (abscissa) and distance of the stream to the accretor in units of the Roche-lobe radius of the accretor (ordinate), when $f_{\text{sync}} = 1$. The red-dashed line indicates the radius of closest approach of the stream in terms of the Roche-lobe radius of the accretor. The orange lines are contour lines of equal spacing between 1.0 and 1.1. For a system with these properties, the specific angular momentum of the stream is generally higher than at the radius of closest approach, but the change in specific angular momentum of the stream is at maximum ~ 10 per cent, specifically at low mass-ratios ($q_{\text{acc}} > 10$) and furthest away from the accretor ($d_{\text{stream-accrator}} = 1.0R_{\text{Roche-Lobe,accrator}}$). At high mass-ratios ($q_{\text{acc}} > 10$), the maximum change over the length of the stream is less (< 5 per cent). This indicates that direct-impact accretion is more efficient the larger the accretor is, but the increase in torque is marginal (up to ~ 10 per cent).

mass-ratio ($q_{\text{acc}} < 0.1$, significantly lower than in the cold-stream case), either with $f_{\text{sync}} < 0.4$ or with $f_{\text{sync}} > 1.5$ (Fig. 19).

Sub-synchronous donors show a general increase of r_{min} with decreasing synchronicity factor. This is due to the initially negative transversal velocity from the sub-synchronous rotation directing the stream further away from the accretor. This eventually leads to a fraction of the stream escaping from the system, but for very sub-synchronous rotating donors many trajectories self-intersect.

At low mass-ratios, super-synchronous donors show a general decrease of r_{min} with increasing synchronicity factor, but this behaviour turns around for highly super-synchronous donors ($f_{\text{sync}} > 1.7$) at low mass ratios ($q_{\text{acc}} < 0.1$). This is because part of the stream for these systems starts accreting onto the donor, and the trajectories that do still accrete onto the accretor on average have a large radius of closest approach. This region of parameter space contains many (self-)intersecting trajectories (Fig. 20), and since we do not treat intersecting orbits differently, this indicates that this region requires a more sophisticated approach than our current one.

We show the ratio of $r_{\text{circ}}/r_{\text{min}}$ in our high thermal-velocity (hot) calculations in Fig. 17.

At high mass-ratios ($q_{\text{acc}} > 1$), while as a function of mass ratio the results are similar to the low thermal-velocity (cold) case, i.e. with higher the mass ratio a lower $r_{\text{circ}}/r_{\text{min}}$, the behaviour as a function of synchronicity is now reversed. The lower the synchronicity, the lower the ratio $r_{\text{circ}}/r_{\text{min}}$, indicating that the trajectories on averages at the radius of closest approach are similar to circular orbits at that radius, and vice versa.

At small mass-ratios ($q_{\text{acc}} < 1$) the behaviour is similar as above, but from $q_{\text{acc}} \leq 0.4$ the sub-synchronous systems get an increasingly high ratio $r_{\text{circ}}/r_{\text{min}}$ with decreasing mass ratio q_{acc} . This coincides with regions of the parameter space where part of the stream either escapes from the system, or starts accreting onto the donor. The re-

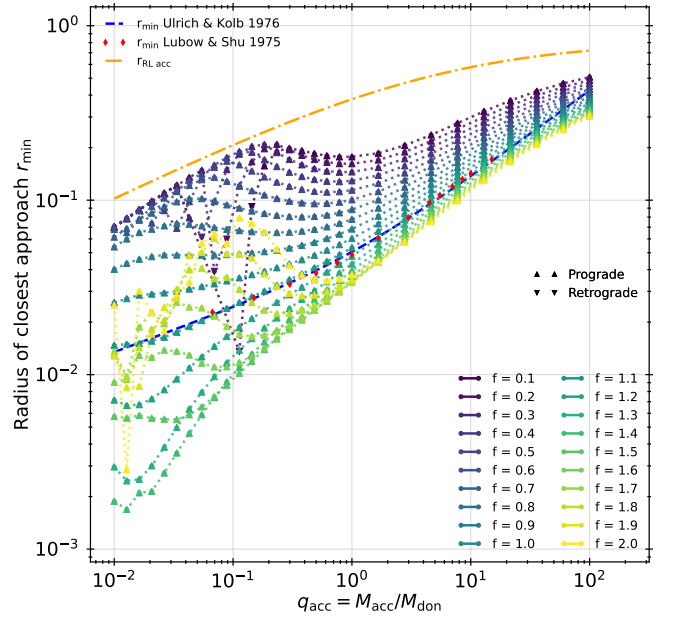


Figure 16. As Fig. 10, but with $v_{\text{thermal}} = 10^{-0.5}$.

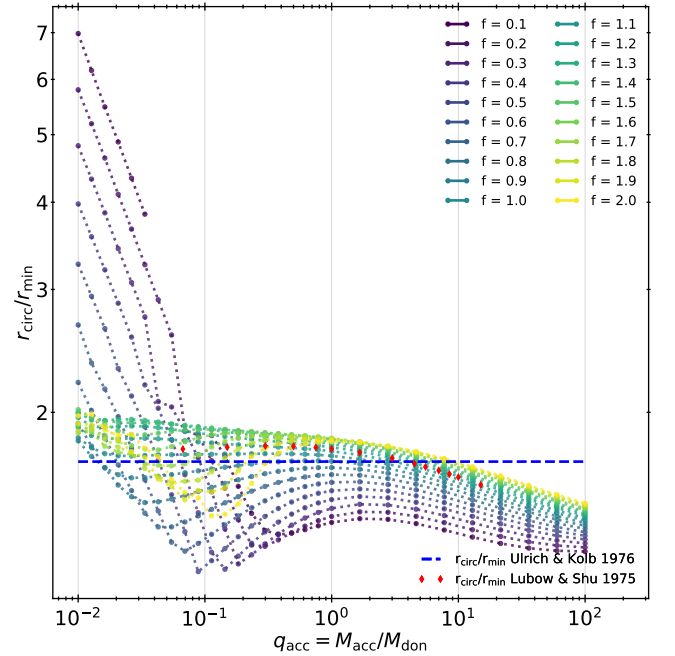


Figure 17. As Fig. 11, but with $v_{\text{thermal}} = 10^{-0.5}$.

maintaining trajectories that barely do not escape often fall back into the Roche-lobe of the accretor near radially, or they find their radius of closest approach very early in their trajectory. For these trajectories, the first radius of closest approach is potentially not suitable to determine the angular momentum of the ring that would form when the stream circles around the accretor and hits itself.

We show the ratio of final and initial specific angular momenta of self-accreting material in our high thermal-velocity (hot) calculations in Fig. 18. While again there are two distinct regions of positive and negative torque of self-accreting material, both regions are smaller

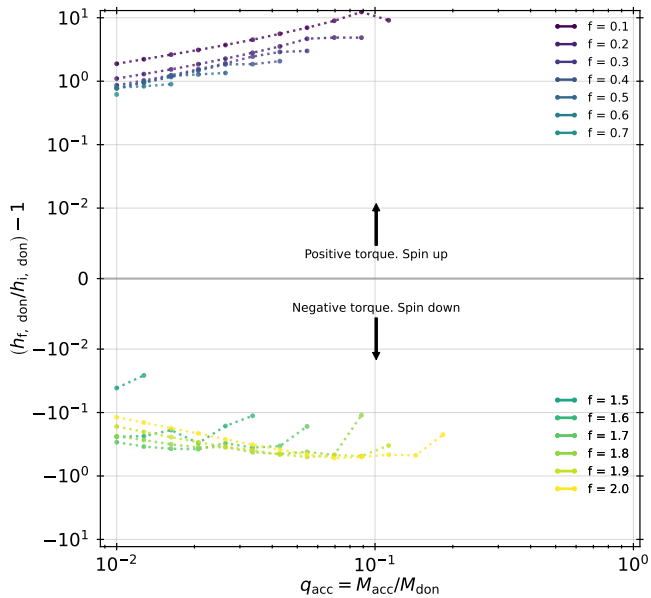


Figure 18. As Fig. 12, but with $v_{\text{thermal}} = 10^{-0.5}$.

and require a higher degree of asynchronicity (i.e. $f_{\text{sync}} > 1.5$) and/or a lower mass ratio ($q_{\text{acc}} < 0.1$) to self-accrete. Systems with super-synchronous that self-accrete tend to experience a higher torque for a given mass ratio, e.g. for $q_{\text{acc}} = 0.01$, $h_{\text{don}, i}/h_{\text{don}, i-1} > -10^{-1}$ for $v_{\text{thermal}} = 10^{-0.5}$ compared to $h_{\text{don}, i}/h_{\text{don}, i-1} = [-10^{-2}, -10^{-1}]$. The angles of incidence of these trajectories with the donor are much larger, nearing perpendicular to its surface.

In Fig. 19 we show the fractions of trajectories in each classification for the hot stream calculations. Fig. 19 (a) shows that compared to our low thermal-velocity (cold) results (Fig. 13), a larger fraction of mass ratios and synchronicity factors accrete onto the accretor, e.g. systems with $0.1 < q_{\text{acc}} < 10$ and $f_{\text{sync}} > 1.5$ or < 0.5 now accrete onto the accretor instead of onto the donor in the low thermal-velocity case ($v_{\text{thermal}} = 10^{-3.0}$). This is mainly attributed to the larger initial radial velocity, which gives the particles more momentum to start with and make it more difficult to change the course of their trajectories. This, in turn, leads to a smaller region of the parameter space in q_{acc} and f_{sync} that accretes back onto the donor. Fig. 19 (c) shows the fraction of trajectories that escapes as a function of q_{acc} and f_{sync} . While at low ($v_{\text{thermal}} = 10^{-3.0}$) thermal-velocity (cold) there is no trajectory that escapes, the high ($v_{\text{thermal}} = 10^{-0.5}$) thermal-velocity allows trajectories to pass the accretor and escape through the Lagrange point behind the accretor (at $x > x_{\text{acc}}$). This primarily occurs in sub-synchronous systems, again due to the Coriolis force accelerating the particle towards positive x . Overall, the data in Fig. 19 (a) and (b) show that instead of the sharp transition between accretion onto accretor and self-accretion, there is a much more gradual transition between the regions where the fractions transition from 0 to 1 over a larger range of parameters. This is because the high thermal-velocity leads to a wide stream, i.e. a wider range of initial positions around L1 for our trajectories for a given system. In systems with e.g. $q_{\text{acc}} = 0.1$ and $f_{\text{sync}} = 1.9$, about half of the trajectories that make up the stream accrete onto the donor, and half accrete onto the accretor. Moreover, some trajectories fail to stay accurate within the given minimum time step, but the total fraction of the failing systems is negligible, and they only occur in small regions.

Fig. 20 shows the intersection fractions for high thermal-velocity

(hot, $v_{\text{thermal}} \approx 0.32$) mass transfer. The structure of the figure is the same as in Fig. 14.

We find that the self-intersecting orbits again occur on the edges of the transition regions between accretion onto the donor and accretion onto the accretor. The fraction itself is not always high, due to the stream being wider and parts the transition region is more gradual (i.e. for a wider range in f_{sync} , q_{acc} , parts of the stream can accrete onto different regions). For sub-synchronous rotation ($f_{\text{sync}} < 0.75$) the region of parameter space where self-accretion occurs is narrow and is more confined to the transition region than self-accretion in super-synchronous ($f_{\text{sync}} > 1.75$) rotating systems. Super-synchronous systems with high-thermal velocity streams have very wide streams, but the asynchronous velocity offset is lower than in the equivalent sub-synchronous configurations ($f_{\text{sync}} < 1.75$, Fig. 3). This leads to trajectories in a larger region in the parameter space self-intersecting. Intersection with other trajectories again coincides with regions of self-intersection, where for sub-synchronous systems the regions overlap strongly but for super-synchronous the region where trajectories intersect with others extends to a larger part of the parameter space ($q_{\text{acc}} < 0.5$ and $f_{\text{sync}} > 1.25$). The increase in stream diameter in this leads to the initial conditions of each trajectory to be sufficiently different to cross at high angles of incidence ($\theta_{\text{intersect}} > 45^\circ$).

Overall, the regions of self-intersection and other-intersection are confined to regions of low mass-ratios ($q_{\text{acc}} < 0.5$), due to the higher radial velocity that occurs at high-thermal velocity, which gives the stream more momentum and makes it harder to deflect or rotate. Only for low mass-ratios is the donor massive enough to turn the trajectories and lead to (self-)intersections.

5 DISCUSSION

We use binary population synthesis to evolve populations of binary systems and record their properties during mass transfer. We do this to find the ranges of the mass ratios of the accretor, q_{acc} , synchronicity factors of the donor, f_{sync} , and thermal velocities v_{thermal} of the stream, that we should cover in our ballistic stream trajectory calculations. At the same time we use these results as a motivation for this study. Most notably, we find that mass transfer takes place with non-synchronous donors for a significant fraction of either mass transferred (≈ 90 per cent), as well as time spent transferring mass (≈ 60 per cent, Fig. 9). We find that the approximation of static tides does not always hold, especially the fraction of mass transferred while the static approximation fails is significant (≈ 10 per cent). This indicates that mass transfer in those systems occurs in a time-dependent potential, the effects of which are not captured by our modelling approach and these systems likely require detailed stellar evolution models and time-averaging to model the mass transfer correctly. We note that, while the results shown in Section 4.1 indicate the extent of the parameters relevant to this study, they should be used just for that. We currently calculate the population statistics for a starburst population at a specific metallicity, and we do not convolve with any star formation rate. This means that our population results are not a directly observable quantity, even if the assumption of a single metallicity is not entirely wrong for populations of dwarfs in the solar neighbourhood (Haywood 2001). Moreover, our results depend on the details of the population synthesis calculations. Changes in, e.g., tidal interaction physics (Mirouh et al. 2023; Preece et al. 2022) or birth distributions (Moe & Stefano 2017; Moe et al. 2019) of the binary components will change our results, although the extent to which is not clear.

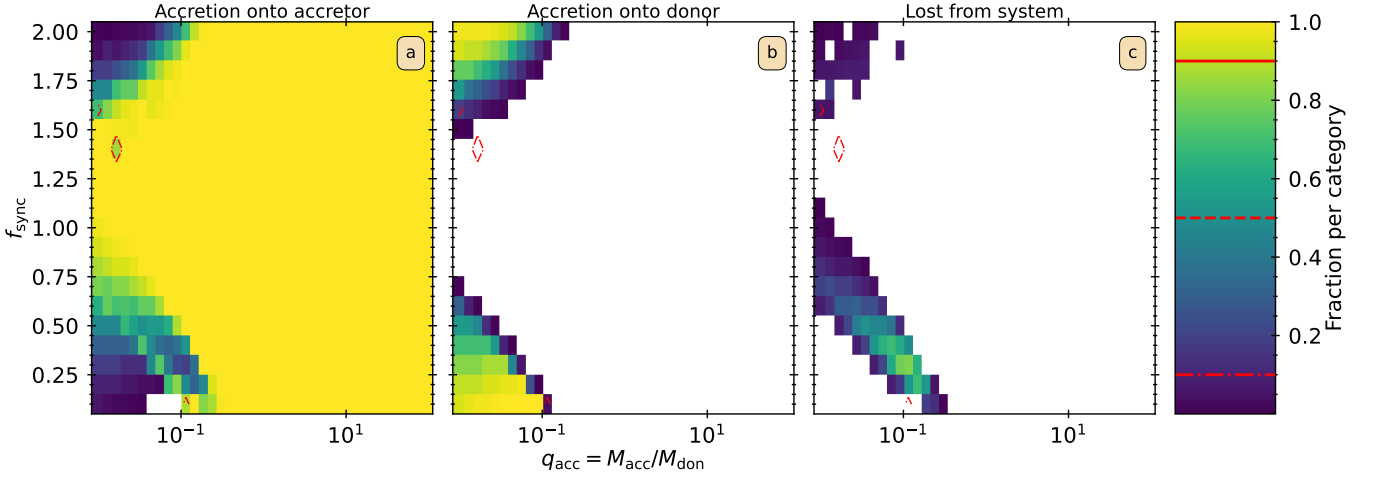


Figure 19. As Fig. 13, but with $v_{\text{thermal}} = 10^{-0.5}$.

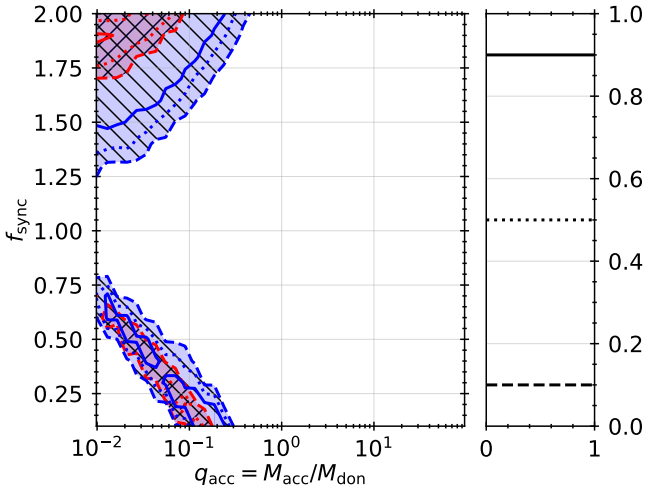


Figure 20. As Fig. 14, but with $v_{\text{thermal}} = 10^{-0.5}$.

Recently Davis et al. (2013, 2014) performed calculations with a similar approach to ours. While they don't supply a data-release, the behaviour of their stream models is described in some cases. They find that, in all cases of self-accretion, the donor experiences a positive torque, effectively spinning up the donor and removing angular momentum from the orbit. This agrees with the results of Sepinsky et al. (2010), as well as with those of Belvedere et al. (1993). The focus of all these studies is on sub-synchronous donors. We find that self-accretion onto super-synchronous donors lead to a spin-down of the donor. Our results imply that if a donor rotates asynchronously and self-accretes, this self-accretion always works to synchronise the donor even if it rotates super-synchronously.

We capture the effects of a large mass transfer stream cross-section by simulating a set of trajectories with initial position offsets along the stream. We treat these trajectories as individual, and we do not include any interaction between these trajectories. In some cases, however, the trajectories along the mass stream intersect at large angles with other trajectories (Warner & Peters 1972). Realistically, these would be swept up by parts of the stream with a higher density and momentum (Flannery & Faulkner 1975). We track whether tra-

jectories intersect with either themselves or with others (Section 3.4) and we find self-intersection and intersection with other trajectories (at angles larger than the threshold) occurs primarily in the transition regions between accretion onto the accretor and accretion onto the donor (Figures 14 and 20). Especially in the high thermal-velocity (hot) stream super-synchronous cases we find that where a high fraction of intersection with other trajectories takes place ($f_{\text{sync}} > 1.25$ and $q_{\text{acc}} < 0.5$) extends to a larger part of the parameter space than the region where self-intersection occurs ($f_{\text{sync}} > 1.75$ and $q_{\text{acc}} < 0.25$, Fig. 20). The very wide stream causes the particles along it to have a large spread in initial conditions and to follow significantly varying trajectories. We currently do not post-process any of these trajectories to alter their outcome or to reject them based on intersection. The regions where a high degree of (self-)intersection occurs likely require an approach that is more sophisticated than approximating the stream by a series of non-interacting ballistic trajectories.

Our ballistic approach imposes some assumptions on the starting conditions of the particle, especially in asynchronous rotating donors. We take the transversal velocity offset due to asynchronous rotation $v_{\text{non-synchronous offset}}$ to scale linearly with the synchronicity factor. Lubow (1993) critiques this approach, and argues that this axisymmetric velocity assumption is not valid (also Limber 1963), and that the problem requires a hydrodynamical analysis. This is based on two studies that look at the gas dynamics of material at L1 in non-synchronous donors using polytropic models for the radiative (Lubow 1979) and convective (Campbell & Papaloizou 1983) stars, specifically the shape of the flow field at L1. They both find that in the linearised and low-asynchronicity case the velocity field tends to zero as it approaches L1, and hence and flow towards L1 slows down and tend to zero before flowing through L1 and increasing. This is in contrast with our assumption of a transverse velocity component linearly dependent on the non-synchronicity factor f_{sync} . A lower velocity offset with the same asynchronous rotation of the donor leads to stream properties that are more like the synchronous case. Because of the initial supersonic velocity relative to the L1 point (Fig. 3) the slow-down can be accompanied by shocks (Lubow 1993). The heating of the shock dissipation could change the initial properties of the stream (e.g. increase the local temperature at L1), and could be observable as an excess luminosity around L1. With observations of mass-transferring systems it might be possible to

discern whether this slow-down to L1 actually occurs, and whether mass-stream trajectories behave like those in synchronous systems even for asynchronous donors.

The aim of this paper was to include the effects of non-synchronous rotation of the donor on the particles in the mass transfer stream in the ballistic approach, where we treat the accretor as a point particle with no physical size. Our method, however, is suitable for extensions like treating direct impact accretion onto the accretor and adding properties of the particle during its flight to the interpolation dataset, and the inclusion of additional physical effects like post-Newtonian potentials for the accretor (Kramarev & Yudin 2023), the effects of kinematic acceleration (Kruszewski 1963) or those of irradiation by the secondary (Podsiadlowski & Rees 1994; Drechsel et al. 1995; Phillips & Podsiadlowski 2002) on the critical surface of the donor.

6 CONCLUSIONS

Motivated by the lack of publicly available data of stream properties in systems with non-synchronously rotating donor stars, we hereby present our results of ballistic trajectory calculations. We calculate ballistic trajectories with varying mass ratio q_{acc} , synchronicity factor f_{sync} and initial thermal-velocity v_{thermal} , and we assume the accretor radius is infinitely small. We make use of binary population synthesis to inform us of the ranges of the initial parameters of the ballistic calculations and to provide further motivation for the importance of this study and the need for a publicly accessible data set on ballistic trajectories for non-synchronous donors.

The main results of our study are summarised below.

(i) Our binary population calculations with metallicity $Z = 0.02$ indicate that a large fraction of binary systems transfer mass sub-synchronously, but they transfer more mass (90.14 per cent) sub-synchronously than spend time doing so (62.44). Only a very low fraction of systems transfers mass super synchronously (< 0.07 per cent mass transferred and < 0.02 per cent time spent transferring mass). Moreover, while only a small fraction of time is spent during which the static tide approximation breaks down, a non-negligible fraction of mass (12.64 per cent) is transferred when the donor experiences a dynamic potential. This does, however, mean that the static potential approximation is valid for the majority (87.36 per cent) of mass transferred with sub-synchronously rotating donors.

(ii) Our ballistic trajectory calculations indicate that at low initial thermal-velocity (cold, $v_{\text{thermal}} = 10^{-3.0}$) there are clear distinctions between accretion onto the accretor and accretion onto the donor within the parameter space of q_{acc} and f_{sync} , and no trajectories escape from the system. The minimum radius of approach can be as low as 10^{-3} , indicating a near head-on stream. A larger region in the $(q_{\text{acc}}, f_{\text{sync}})$ parameter space leads to accretion onto the donor for super-synchronous donors ($f_{\text{sync}} > 1$ and $q_{\text{acc}} < 100$) than for sub-synchronous donors ($f_{\text{sync}} < 0.75$ and $q_{\text{acc}} < 5$), but the change in specific angular momentum of the self-accreting stream is overall lower for super-synchronous donors. Both for sub-synchronous as for super-synchronous donors the self-accretion always works synchronising. We find that intersecting trajectories only occur at the edge of the transition region between accretion onto the accretor and accretion onto the donor and that the self-intersection regions overlap with that of intersection with other trajectories.

(iii) High initial thermal-velocities (hot, $v_{\text{thermal}} = 10^{-0.5}$) correspond to a wider mass stream, and lead to a less sharp transition between the regions of accretion onto the donor and accretion onto the accretor. Fewer configurations of q_{acc} and f_{sync} , i.e. $f_{\text{sync}} > 1.5$ and $q_{\text{acc}} < 0.2$ for super-synchronous donors and $f_{\text{sync}} < 0.75$

and $q_{\text{acc}} < 0.1$ for sub-synchronous donors, lead to accretion onto donor because of the larger initial radial velocity of the stream that makes it more difficult to deflect the stream. We find some trajectories can escape the system through the Lagrange point behind the accretor ($x > x_{\text{acc}}$), especially in systems with a sub-synchronous donor. Intersecting trajectories again occur at the edge of the transition region, but for super-synchronous donors the intersection with other trajectories occurs for a larger part of the parameter space than self-intersecting orbits, i.e. $f_{\text{sync}} > 1.25$ and $q_{\text{acc}} < 0.5$ for intersection with other trajectories and $f_{\text{sync}} > 1.7$ and $q_{\text{acc}} < 0.1$ for self-intersection.

Our results are useful for orbital evolution and mass transfer calculations, including determining the formation and properties of accretion disks. They can be used in stellar evolution and population synthesis code, and they are available online upon publication of the paper.

ACKNOWLEDGEMENTS

DDH thanks the UKRI and the University of Surrey for the funding grant H120341A, and thanks Arman Aryaeipour, Dominika Hubová, Giovanni Mirouh, Ondřej Pejcha, Natalie Rees and Mathieu Renzo for useful discussions. RGI thanks STFC for funding grants [ST/R000603/1](https://doi.org/10.5281/zenodo.7007591) and [ST/L003910/2](https://doi.org/10.5281/zenodo.7007591).

DATA AVAILABILITY

We make our ballistic trajectory integration code, as well as the interpolation tables for the stream properties and the exploration data generated through population synthesis available on <https://doi.org/10.5281/zenodo.7007591> upon publication.

REFERENCES

- Avni Y., 1976, *The Astrophysical Journal*, 209, 574
 Avni Y., Schiller N., 1982, *The Astrophysical Journal*, 257, 703
 Belvedere G., Lanzafame G., Molteni D., 1993, *280*, 525
 Blaauw A., 1961, *Bulletin of the Astronomical Institutes of the Netherlands*, 15, 265
 Campbell C. G., Papaloizou J., 1983, *Monthly Notices of the Royal Astronomical Society*, 204, 433
 Claeys J. S. W., Pols O. R., Izzard R. G., Vink J., Verbunt F. W. M., 2014, *Astronomy & Astrophysics*, 563, A83
 Davis P. J., Siess L., Deschamps R., 2013, *Astronomy and Astrophysics*, 556, A4
 Davis P. J., Siess L., Deschamps R., 2014, *Astronomy and Astrophysics*, 570, A25
 De Marco O., Izzard R. G., 2017, *Publications of the Astronomical Society of Australia*, 34
 Dermine T., Jorissen A., Siess L., Frankowski A., 2009, *Astronomy & Astrophysics*, 507, 891
 Dosopoulou F., Kalogera V., 2016, *The Astrophysical Journal*, 825, 70
 Dosopoulou F., Naoz S., Kalogera V., 2017, *The Astrophysical Journal*, 844, 12
 Drechsel H., Haas S., Lorenz R., Gayler S., 1995, *294*, 723
 Flannery B. P., Faulkner J., 1975, *Monthly Notices of the Royal Astronomical Society*, 170, 325
 Ghodla S., Eldridge J. J., Stanway E. R., Stevance H. F., 2023, *Monthly Notices of the Royal Astronomical Society*, 518, 860
 Hairer E., Nørsett S. P., Wanner G., 2008, *Solving Ordinary Differential Equations I: Nonstiff Problems*. Springer Science & Business Media
 Hameury J.-M., 2020, *Advances in Space Research*, 66, 1004

- Haywood M., 2001, *Monthly Notices of the Royal Astronomical Society*, 325, 1365
- Hendriks D. D., Izzard R. G., 2023, *Journal of Open Source Software*, 8, 4642
- Hubová D., Pejcha O., 2019, *Monthly Notices of the Royal Astronomical Society*, 489, 891
- Hurley J. R., Pols O. R., Tout C. A., 2000, *Monthly Notices of the Royal Astronomical Society*, 315, 543
- Hurley J. R., Tout C. A., Pols O. R., 2002, *Monthly Notices of the Royal Astronomical Society*, 329, 897
- Hut P., 1981, *Astronomy and Astrophysics*, 99, 126
- Izzard R. G., Jermyn A. S., 2022, *Monthly Notices of the Royal Astronomical Society*
- Izzard R. G., Tout C. A., Karakas A. I., Pols O. R., 2004, *Monthly Notices of the Royal Astronomical Society*, 350, 407
- Izzard R. G., Dray L. M., Karakas A. I., Lugaro M., Tout C. A., 2006, *Astronomy & Astrophysics*, 460, 565
- Izzard R. G., Glebbeek E., Stancliffe R. J., Pols O. R., 2009, *Astronomy and Astrophysics*, 508, 1359
- Izzard R. G., Preece H., Jofre P., Halabi G. M., Masseron T., Tout C. A., 2018, *Monthly Notices of the Royal Astronomical Society*, 473, 2984
- Jermyn A. S., et al., 2023, *The Astrophysical Journal Supplement Series*, 265, 15
- Kashi A., Soker N., 2011, *Monthly Notices of the Royal Astronomical Society*, 417, 1466
- Kramarev N., Yudin A., 2023, *Monthly Notices of the Royal Astronomical Society*, 522, 626
- Kruszewski A., 1963, *Acta Astronomica*, 13, 106
- Kruszewski A., 1964a, *Acta Astronomica*, 14, 231
- Kruszewski A., 1964b, *Acta Astronomica*, 14, 241
- Kruszewski A., 1967, *Acta Astronomica*, 17, 297
- Limber D. N., 1963, *The Astrophysical Journal*, 138, 1112
- Lubow S. H., 1979, *The Astrophysical Journal*, 229, 1008
- Lubow S. H., 1993, in Sahade J., McCluskey G. E., Kondo Y., eds, *Astrophysics and Space Science Library, The Realm of Interacting Binary Stars*. Springer Netherlands, Dordrecht, pp 25–37, doi:10.1007/978-94-011-2416-4_5, https://doi.org/10.1007/978-94-011-2416-4_5
- Lubow S. H., Shu F. H., 1975, *The Astrophysical Journal*, 198, 383
- Mehlhorn K., Näher S., 1994
- Meyer F., Meyer-Hofmeister E., 1983, *Astronomy and Astrophysics*, 121, 29
- Mirouh G. M., Hendriks D. D., Dykes S., Moe M., Izzard R. G., 2023, *Monthly Notices of the Royal Astronomical Society*, p. stad2048
- Moe M., Stefano R. D., 2017, *The Astrophysical Journal Supplement Series*, 230, 15
- Moe M., Kratter K. M., Badenes C., 2019, *The Astrophysical Journal*, 875, 61
- Moulton F. R., 1914, *An Introduction to Celestial Mechanics*. Macmillan, https://ui.adsabs.harvard.edu/abs/1914icm.book.....M
- Nomoto K., 1986, *Progress in Particle and Nuclear Physics*, 17, 249
- Ogilvie G. I., 2014, *Annual Review of Astronomy and Astrophysics*, 52, 171
- Osaki Y., Hirose M., Ichikawa S., 1993, *Accretion Disks in Compact Stellar Systems*, p. 272
- Ovenden M. W., Roy A. E., 1961, *Monthly Notices of the Royal Astronomical Society*, 123, 1
- Papaloizou J., Pringle J. E., 1977, *Monthly Notices of the Royal Astronomical Society*, 181, 441
- Pejcha O., Metzger B. D., Tomida K., 2016, *Monthly Notices of the Royal Astronomical Society*, 461, 2527
- Phillips S. N., Podsiadlowski Ph., 2002, *Monthly Notices of the Royal Astronomical Society*, 337, 431
- Plavec M., 1958, in *Liege International Astrophysical Colloquia*. pp 411–420
- Podsiadlowski P., Rees M. J., 1994, *AIP Conference Proceedings*, 308, 71
- Pols O. R., Schröder K.-P., Hurley J. R., Tout C. A., Eggleton P. P., 1998, *Monthly Notices of the Royal Astronomical Society*, 298, 525
- Postnov K. A., Mironov A. I., Lutovinov A. A., Shakura N. I., Kochetkova A. Y., Tsygankov S. S., 2015, *Monthly Notices of the Royal Astronomical Society*, 446, 1013
- Preece H. P., Hamers A. S., Neunteufel P. G., Schafer A. L., Tout C. A., 2022, *The Astrophysical Journal*, 933, 25
- Pringle J. E., Rees M. J., 1972, *Astronomy and Astrophysics*, 21, 1
- Raymer E., 2012, *Monthly Notices of the Royal Astronomical Society*, 427, 1702
- Renzo M., et al., 2019, *Astronomy & Astrophysics*, 624, A66
- Riley J., et al., 2022, *The Astrophysical Journal Supplement Series*, 258, 34
- Ritter H., 1988, *Astronomy and Astrophysics*, 202, 93
- Ruiter A. J., Belczynski K., Sim S. A., Hillebrandt W., Fink M., Kromer M., 2010, in Kalogera V., van der Sluys M., eds, *American Institute of Physics Conference Series Vol. 1314, International Conference on Binaries: In Celebration of Ron Webbink's 65th Birthday*. pp 233–238 (arxiv:1009.3661), doi:10.1063/1.3536375
- Savonije G. J., 1978, *Astronomy and Astrophysics*, 62, 317
- Sepinsky J. F., Willems B., Kalogera V., 2007, *The Astrophysical Journal*, 660, 1624
- Sepinsky J. F., Willems B., Kalogera V., Rasio F. A., 2010, *The Astrophysical Journal*, 724, 546
- Shakura N. I., Sunyaev R. A., 1973, 24, 337
- Shao Y., Li X.-D., 2014, *The Astrophysical Journal*, 796, 37
- Tauris T. M., Takens R. J., 1998, *Astronomy and Astrophysics*, 330, 1047
- Tout C. A., Aarseth S. J., Pols O. R., Eggleton P. P., 1997, *Monthly Notices of the Royal Astronomical Society*, 291, 732
- Tsantilas S., Rovithis-Livaniou H., 2006, 349, 355
- Ulrich R. K., Burger H. L., 1976, *The Astrophysical Journal*, 206, 509
- Vanbeveren D., 1977, *Astronomy and Astrophysics*, 54, 877
- Virtanen P., et al., 2020, *Nature Methods*, 17, 261
- Warner B., Peters W. L., 1972, *Monthly Notices of the Royal Astronomical Society*, 160, 15
- Zahn J. P., 1975, *Astronomy and Astrophysics*, 41, 329
- Zahn J. P., 1977a, *Astronomy and Astrophysics*, 57, 383
- Zahn J.-P., 1977b, *Astronomy and Astrophysics*, 500, 121
- Zahn J. P., 2008, in *EAS Publications Series*. eprint: arXiv:0807.4870, pp 67–90, doi:10.1051/eas:0829002, https://ui.adsabs.harvard.edu/abs/2008EAS....29...67Z

APPENDIX A: DESCRIPTION OF OUTPUT DATASETS

The ballistics stream trajectory summary datasets contain the parameters described in Table A1, along with meta-data regarding indices and global configurations. These datasets can be interpolated on and implemented in other binary stellar evolution codes to include the effect explored in our paper and the subsequent changes in the mass transfer properties like the torque on the orbit, the fraction of self accretion.

APPENDIX B: LAGRANGE POINTS AS A FUNCTION OF SYNCHRONICITY

With equation 4 we calculate the first three Lagrange points, the donor for the synchronicity factors f_{sync} and mass ratios q_{acc} . We calculate these in the non-inertial reference frame centred on the donor and transform this to the non-inertial reference frame centred on the centre of mass of the system (Section 2.1). In Fig. B1 we show the x -coordinate of the first three Lagrange points for both of these frames.

This paper has been typeset from a $\text{\TeX}/\text{\LaTeX}$ file prepared by the author.

Name	Description	Reference	Input/Output
Initial thermal velocity $\log_{10}(v_{\text{thermal}})$	Initial thermal velocity of particles at L1.	Section 2.2.1 and equation 7	Input
Synchronicity factor f_{sync}	Synchronicity factor of the donor.	Section 2.1 and equation 3	Input
Mass ratio q_{acc}	Mass ratio of the accretor, $q_{\text{acc}} = M_{\text{accretor}}/M_{\text{donor}}$.		Input
Total weight successful w_{succes}	Total weight of the successful trajectory calculations.	Section 3.3 and equation 22	Output
Total weighted fraction self-intersecting trajectories $f_{\text{self intersect}}$	Total weighted fraction of the valid trajectories that self-intersect.	Section 3.4	Output
Total weighted fraction other-intersecting trajectories $f_{\text{other intersect}}$	Total weighted fraction of the valid trajectories that intersect with other orbits at angles above the threshold $\theta_{\text{threshold}}$.	Section 3.4	Output
Accretor accretion fraction β_{acc}	Total weighted fraction of trajectories that accrete onto the accretor.	Section 3.3 and equation 20	Output
Self accretion fraction β_{don}	Total weighted fraction of trajectories that accrete back onto the donor.	Section 3.3	Output
Initial specific angular momentum w.r.t donor $h_{i, \text{don}}$	Average weighted initial specific angular momentum of the mass stream with respect to the donor.	Section 3.5.1 and equation 27	Output
Self-accretion specific angular momentum factor $h_{f, \text{don}}/h_{i, \text{don}}$	Average weighted ratio of final and initial specific angular momentum of the mass that accretes back onto the donor.	Section 3.5.1 and equation 27	Output
Radius of closest approach r_{min}	Average weighted radius of closest approach to the accretor of the mass transfer stream for accretion onto accretor.	Section 3.5	Output
Circularisation radius r_{circ}	Average weighted radius of circularisation based on the angular momentum content of the stream at the radius of closest approach for accretion onto accretor.	Section 3.5 and equation 24	Output
Stream orientation	Average weighted pro- or retrograde orientation of the stream.		Output
Specific angular momentum along the stream at i-th radius $h_{\text{stream } i}$	Averaged weighted specific angular momentum of the stream at distance $d_{\text{stream } i}$. For radii that are smaller than the radius of closest approach r_{min} , this quantity is set to 0. For donor-accretion this quantity is filled with a dummy value. The distances $d_{\text{stream } i}$ are expressed in units of the Roche-lobe radius of the accretor.	Section 3.5 and equation 26	Output

Table A1. Parameters included in the output datasets. The Input/Output column indicates whether this parameter is an input parameter to the interpolation table, or an output quantity.

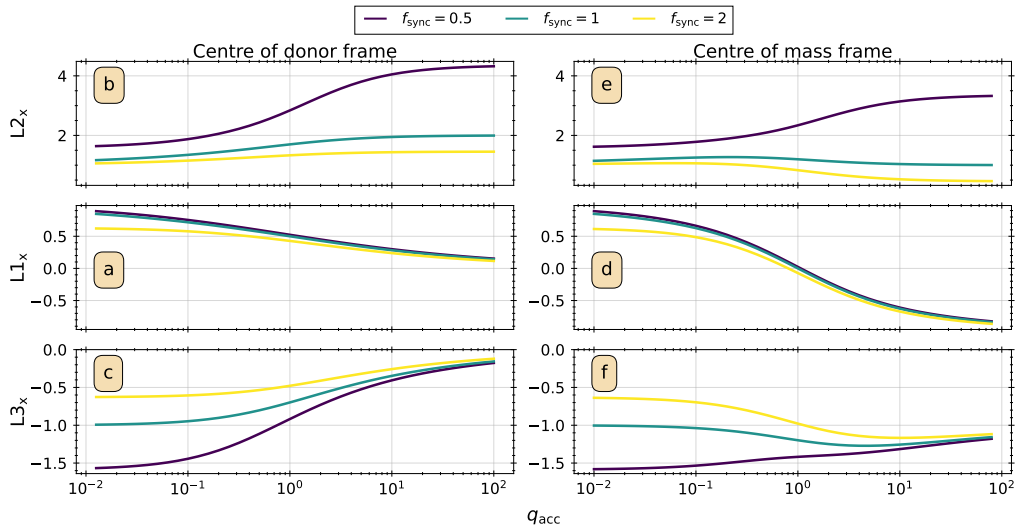


Figure B1. x -coordinates of the first three Lagrange points of the donor ($L1_x$, $L2_x$, $L3_x$) in the reference frame centred on the donor (b, a and c respectively) and the reference frame centred on the centre of mass of the binary system (e, d and f respectively) (Section 2.1).